On a phase-field approach to model fracture of small intestine walls

Journal Article

Author(s):
Nagaraja, Sindhu; Leichsenring, Kay; Ambati, Marreddy; De Lorenzis, Laura (iD); Böl, Markus

Full length article

On a phase-field approach to model fracture of small intestine walls

Sindhu Nagaraja [a], Kay Leichsenring [b], Marreddy Ambati [c], Laura De Lorenzis [a], Markus Böl [b,*]

[a] *Department of Mechanical and Process Engineering, ETH Zürich, Zürich CH-8092, Switzerland*
[b] *Institute of Mechanics and Adaptronics, Technische Universität Braunschweig, Braunschweig D-38106, Germany*
[c] *Chair of Computational and Experimental Solid Mechanics, Technische Universität Dresden, Dresden D-01069, Germany*

ARTICLE INFO

ABSTRACT

We address anisotropic elasticity and fracture in small intestine walls (SIWs) with both experimental and computational methods. Uniaxial tension experiments are performed on porcine SIW samples with varying alignments and quantify their nonlinear elastic anisotropic behavior. Fracture experiments on notched SIW strips reveal a high sensitivity of the crack propagation direction and the failure stress on the tissue orientation. From a modeling point of view, the observed anisotropic elastic response is studied with a continuum mechanical model stemming from a strain energy density with a neo-Hookean component and an anisotropic component with four families of fibers. Fracture is addressed with the phase-field approach, featuring two-fold anisotropy in the fracture toughness. Elastic and fracture model parameters are calibrated based on the experimental data, using the maximum and minimum limits of the experimental stress-stretch data set. A very good agreement between experimental data and computational results is obtained, the role of anisotropy being effectively captured by the proposed model in both the elastic and the fracture behavior.

Statement of significance

This article reports a comprehensive experimental data set on the mechanical failure behavior of small intestinal tissue, and presents the corresponding protocols for preparing and testing the samples. On the one hand, the results of this study contribute to the understanding of small intestine mechanics and thus to understanding of load transfer mechanisms inside the tissue. On the other hand, these results are used as input for a phase-field modelling approach, presented in this article. The presented model can reproduce the mechanical failure behavior of the small intestine in an excellent way and is thus a promising tool for the future mechanical description of diseased small intestinal tissue.

1. Introduction

The healthy small intestine (SI), lined with numerous villi and crypts, is the central organ of nutrient utilization, as it is here that both the enzymatic process of breaking down the chyme and the absorption of the usable nutrients takes place. Its peristaltic movements allow long contact times of the chyme with the internal mucosa, to be the innermost layer of the SI wall (SIW). In addition, the SI absorbs up to 80% of the water from the chyme, making it the essential organ for water absorption. Not least, the organ plays an important role in the immune defense. The lymphatic tissue of the SI is therefore able to absorb antigens, trigger specific immune responses and differentiate between beneficial and exogenous intestinal bacteria.

Any form of disturbance in the interplay between electrical, chemical, and/or mechanical variables in the SI leads to imbalances and consequently to disease patterns that severely impair the quality of life of patients and are of great socio-ecological interest. Thus, there are various clinical pictures, some of which can cause unspecific pain in the SI. Their spectrum ranges from simple constipation and inflammation to severe chronic inflammation, intestinal ulcers, and intestinal obstruction. One of the most important visceral medical diseases is the acute abdomen, which accounts for up to 40% of all emergency surgical hospital admissions. This often

life-threatening condition requires a high level of clinical experience [17,34,63]. It is a threatening disease with very severe abdominal pain, which requires immediate clarification because of the tendency to worsen rapidly, often requiring rapid surgical treatment. A large percentage of the acute abdomen hinders gastrointestinal perforations (GIPs) or secondary peritonitis [20,88]. GIPs cause significant mortality and usually require emergency surgery. Although the development of diagnostic methods and drugs has made enormous progress in recent decades, the morbidity rate has declined only slightly and is between 20% and 60% [76,107].

In principle, all GIPs are based on the loss of the corresponding organ wall stability and the release of intraluminal contents into the abdominal cavity. Following Langell and Mulvihill [58], various underlying causes can be categorized. Many of the GIPs can be found in the intestine. In addition, it was shown that GIPs occur more frequently in newborns in this region [39,70]. In this age range, GIP presents important challenges and a high mortality (15–70%) was reported [28,99]. It is easy to see that the GIP is of high socio-ecological interest to society. However, from a mechanical perspective, it is clear that as the GIP progresses, there are significant structural changes in the organ wall that directly influence the mechanical behavior. Surprisingly, to date no studies investigated these mechanical changes during the course of the disease.

From an anatomical point of view, the SI is divided into three adjacent regions from cranial to caudal, called the ileum, jejunum, and duodenum. Within these regions, the SIW shows a multi-layered structure, with the four layers (from outside to inside) called serosal, muscular, submucosal, and mucosal layer. With regard to the mechanical behavior of the SIW, the different orientations of the collagen and smooth muscle fibers are particularly important, for further details see Section 2.2.

Mechanical experiments to analyse the elastic characteristics of intestine tissue are relatively rare, two types of experiments can be identified: The first type of experiments is performed on intestinal segments to mimic the physiological loading conditions of the organ, while mechanical tests on dissected tissue strips are used to determine position-dependent and layer-specific properties. Experiments on intestine segments are mostly realized as so-called inflation tests. Based on its relatively simple setup, this kind of experiments is predominant in the literature. Thereby, an intestinal organ segment is positioned horizontally between two bearings on which the segment ends are fixed. In the simplest case, the segment is biaxially loaded by applying an intraluminal pressure inside the segment [15,18,23–25,35,62,111,112]. Combining the axial stretching of the SI segment with an inflation leads to a triaxial loading case [26,59,92]. Sun et al. [100] presented a device that is additionally capable of applying a torsional deformation. The advantage of these experiments is their ability to realize physiological load conditions. However, although they can be performed at different positions along the intestine, spatially resolved or even layer-specific analyses are not possible. For more localized analyses of the mechanical behavior, experiments on tissue strips were performed. There are only six studies that perform experiments on dissected strips in the form of uniaxial tension [27,46], shear [19], and biaxial tension experiments [8,61,87]. With the exception of the study by Bellini et al. [8], realizing biaxial experiments within the three regions (duodenum, jejunum, ileum) of the SI, none of the aforementioned analyses on isolated strips investigate position-dependent analyses.

Even after intensive literature research, no studies could be found that characterize the mechanical failure behavior of SI tissue. The majority of such investigations on smooth muscle tissue is realized on aortic tissue. Various types of experiments, ranging from uniaxial/biaxial [51,54,64,96,97,103–105] and shear [97] over tearing/peeling tests [79,96,104,105] to experimental analyses at organ

segment scale such as ring inflation [43–45] and segment inflation tests [38,68] were carried out in this area to determine the failure behavior of the tissue.

The development of constitutive relationships to describe the macroscopic mechanical behavior of SI tissues is an essential step in the systematic numerical investigation of both the physiology and pathophysiology of the SI. Morphological and mechanical studies on various smooth muscle tissues such as the urinary bladder [e.g. 69,90,106], stomach [e.g. 7,52,55], or large intestine [e.g. 13–15], reveal a similar four-layered, mechanically anisotropic hierarchical structure. Based on these similarities, the constitutive modeling of intestinal tissues can benefit from the frameworks developed for other types of biological tissues. Some early works on arteries are reported in Demiray and Vito [22], Fung et al. [32] and Delfino et al. [21]. Hoeg et al. [47] propose constitutive relations for the SI idealized as a pressure vessel undergoing large deformations. Four- or seven-parameter Fung type exponential models have been implemented for the mechanical characterization of large intestine [94], ureter [91], SI [8,25,59]. However, it is well known that these models are not able to accurately represent multiaxial data for SI [93]. Alternatively, a constitutive approach, first introduced for arterial walls, which has become popular is the so-called Holzapfel-Gasser-Odgen (HGO) model, first presented in Holzapfel et al. [50], and further generalized by Gasser and Holzapfel [36]. This approach describes the passive mechanical response of biological tissues by departing from a polyconvex free energy function. The latter is decoupled into isotropic and anisotropic parts which represent the contributions of the ground biological matrix and directional fiber reinforcements, respectively. Anisotropy and some micro-structural information are incorporated through a fiber-reinforced material framework use of structural tensors. Following the HGO model, Carniel et al. [13,14], Ciarletta et al. [19] discuss a hyperelastic framework considering strain energy contributions deriving from the fibers to model the overall anisotropic response of large intestinal tissues, see also Patel et al. [80]. Similar studies are performed in Sokolis and Sassani [95], where a neo-Hookean model with three fiber families is mentioned to be the optimal choice for rat large intestines. Zhao et al. [113] present the constitutive modeling of mouse colorectum, where both bulk and layer specific studies using biaxial tension experiments are carried out. Studies with five different strain energy functions for porcine colon are made in Puértolas et al. [83], where a higher predictive capability of the four fiber model compared to the others is established. More recently, Sokolis [93] study specifically the biomechanical properties of rat SI tissue using inflation/extension tests and a microstructure based formulation containing neo-Hookean matrix and different fiber families.

Numerical approaches studying failure exclusively in SI is hitherto not found in the literature. Several attempts to study failure in other similar tissues have been made. Continuum damage mechanics approaches were adopted to study failure in different fibrous tissues [6,48,60,71,86]. In a similar context, Peña et al. [81] used additionally the experimental data obtained by uniaxial tests on porcine aortic samples to evaluate the model parameters. Cohesive zone modeling for fracture was used in Ferrara and Pandolfi [30] and Noble et al. [73] to model aortic damage. Gasser and Holzapfel [36], Wang et al. [108] and Karimi et al. [53] applied the extended finite element method to study arterial dissection where the nodal degrees of freedom near the crack discontinuity are locally enriched. In another study, Rausch et al. [85] and Ahmadzadeh et al. [1] examined soft tissue failure using a particle based approach. In the past decade, the phase-field modeling approach to fracture originating from the works of Francfort and Marigo [31] and Bourdin et al. [10] has attracted a great deal of attention in the computational fracture mechanics community, due to its numerous advantages over competitor approaches, see
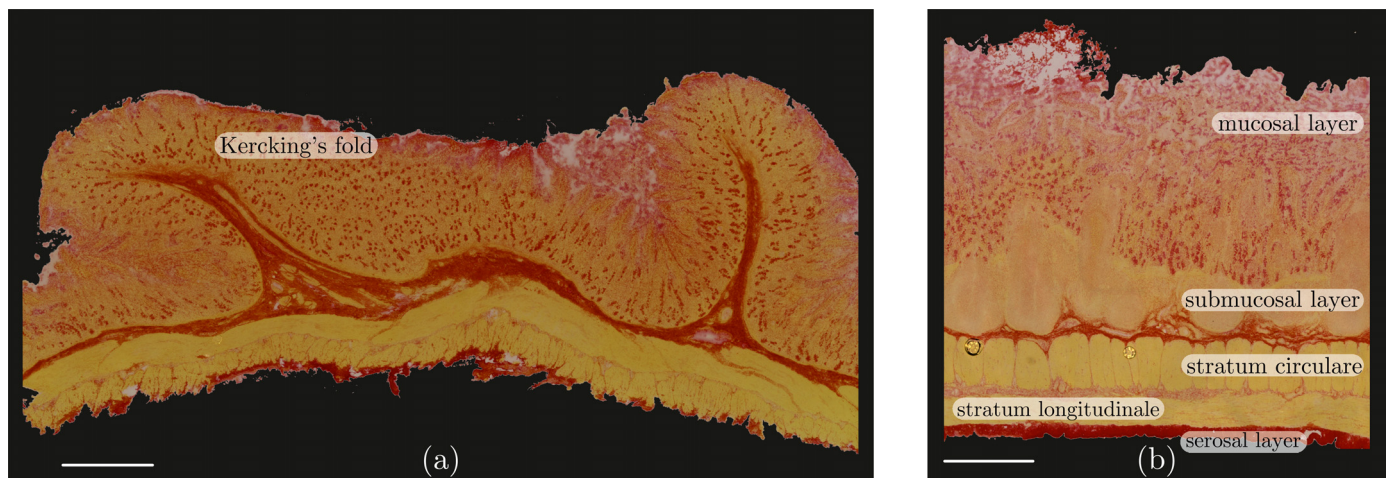
Fig. 1. SIW structure in form of histological sectional image stained with Picro-Sirius red: (a) Histological sectional image illustrating Kerckring's folds and (b) enlargement of the SIW featuring the different layers. Scale Bars: 1 mm.

the review in Ambati et al. [2] and the references therein. Using this framework, tissue fracture studies with specific focus on human artery have been undertaken in Raina and Miehe [84] and Gültekin et al. [40], where phase-field models with a stress-based and an energy-based anisotropic crack driving force, respectively, have been used. A structural tensor based approach to introduce anisotropy in the phase-field model in addition to the anisotropic crack driving force is presented in Gültekin et al. [41] and Gültekin et al. [42]. Despite the extensive literature available on arterial tissue failure, to the best of our knowledge, the potential of the phase-field modeling approach to model fracture in SI tissues has not been exploited until date. In this paper, we aim at filling this gap and investigate phase-field modeling of fracture of SIWs.

2. Materials and methods

2.1. Ethical approval

The study was exempted from ethical committee review according to national regulations (German Animal Welfare Act) as porcine SIs of healthy, female domestic pigs were obtained from a slaughterhouse immediately after animal sacrifice.

2.2. Microstructural aspect of the small intestine wall

From the mechanical point of view, the SIW has remarkable characteristics that are responsible for the functionality of the SI. Essential for this is its microstructure, which consists of four layers (from inside out), see Fig. 1: Mucosal, submucosal, muscular, and serosal layer. The innermost mucosal layer consists of three further layers, the mucosal epithelium as a single-layer acid epithelium, the lamina propria mucosae as reticular connective tissue, and the mucosal lamina, consisting of smooth muscle cells, which are important for intrinsic motility [66]. Particularly striking is the wrinkle structure of the mucosal layer. These wrinkles, the so-called Kerckring's folds enlarge the surface of the layer by a factor of 3. From the microstructural point of view, there are no structures featuring distinct directions, thus this mucosal layer behaves mechanically isotropically. The submucosal layer is a loose connective tissue. In the unstretched state, the collagen fibers feature an orientation of $\pm 30°$ to $\pm 50°$ with respect to the SI's longitudinal axis [33,56,74,75] and show a clear spiralization [29,74]. The consequence of this structure is an initially slowly increasing wall tension with the following exponential increase after uncoiling of the

collagen fibers. In addition, blood vessels, lymphatic vessels, submucosal glands, and the submucosal plexus can be found in this layer. By this layer the mucosal layer is connected with the muscular layer, which in turn consists of two sublayers, the stratum circulare and the stratum longitudinale [5,33,65], which are named according to the smooth muscles' orientation with respect to the longitudinal axis of the SI. The main component of this layer are smooth muscle, collagenous extracellular matrix (ECM), and a relatively low proportion of elastin [29]. The outer surface of the SI is formed by the serosal layer. This serous membrane, which consists of a loose layer of connective tissue, serves, among other things, to reduce friction with other organs.

2.3. Tissue sample dissection and processing

Five ($n = 5$) SIs of female domestic pigs (*Sus scrofa domestica*, age: 5-7 months, mass: 90 to 100 kg) were obtained from a slaughterhouse immediately after animal sacrifice. During transport to the laboratory (and during preparation), the organs were stored at 4°C in calcium-free Krebs solution ([78]: 113 mM NaCl, 4.7 mM KCl, 1.2 mM MgSO$_4$, 25 mM NaHCO$_3$, 1.2 mM KH$_2$PO$_4$, 5.9 mM dextrose, and 1 mM EGTA) to prevent spontaneous contractions, especially during the axial tensile experiments. Thereafter the jejunum, which is located in the caudoventral abdominal cavity of the animal, was isolated, cleaned, and freed from the mesentery, to be attached along the longitudinal axis of the jejunum, see Fig. 2 (a). To obtain a flat specimen, all SIs were cut along the line of the mesentery, from which rectangular tissue strips were prepared depending on their orientation (0°, 30°, 60°, and 90° with respect to the SI's circumferential axis), see (b). All specimen were randomized dissected within the first 50 centimeter of the jenunum. Overall, thirty-nine ($n = 39$) samples were used in this study, divided into two groups, see also Table 1. While the first group (G_u) includes twenty ($n = 20$) un-notched samples, the second one (G_n) consists of nineteen ($n = 19$) samples, which were notched with a depth of 2.28 ± 0.77 mm in the middle of the sample, see (c). All sample dimensions were determined in a post-processing step, using digital images recorded during preparation.

2.4. Tissue strip experiments

All experiments were conducted with a testing machine (Zwick Z010, Zwick GmbH & Co. Ulm, Germany), equipped with a 20 N load cell, cf. Fig. 2 (d). Before performing the axial tensile experiments, the cross-section area A of each of the strips was quanti-
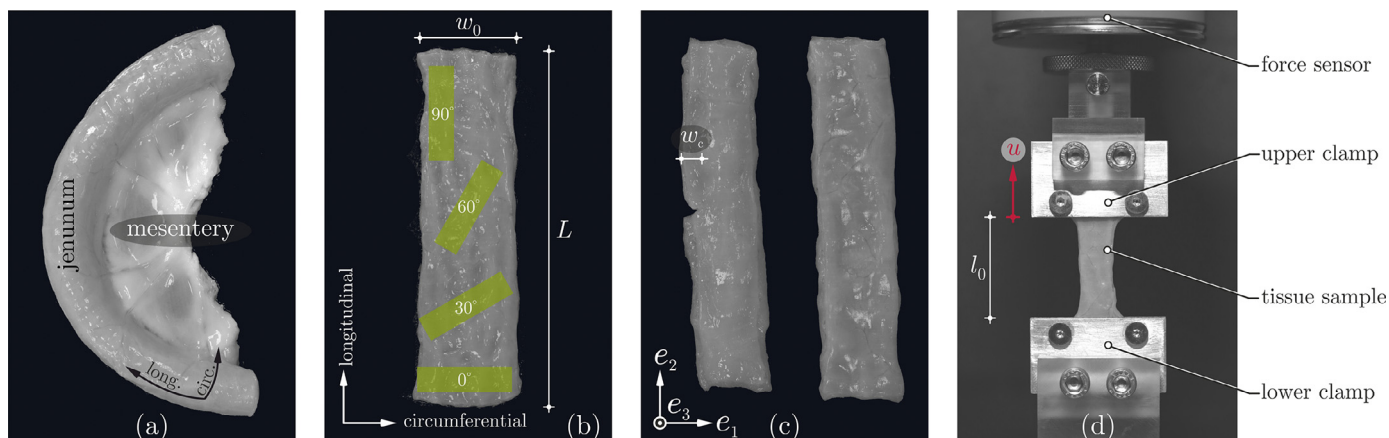
Fig. 2. SI sample processing: (a) Section of the jejunum with attached mesentery, which was removed in a further step. Various tissue orientations (0°, 30°, 60°, and 90° with respect to the SI's circumferential axis) were considered (b) from which two groups (un-notched and notched) were formed, see (c). (d) Experimental setup for the axial tension experiments.

Table 1
Sample number, orientation, and dimensions according to the measures given in Figure 2. Note, the samples' dimensions are given as mean values ± standard deviations (s.d.).

group	no. of samples	orientation [°]	L [mm]	l_0 [mm]	w_0 [mm]	w_c [mm]	t_0 [mm]
G_u	5	0	40.62 ± 0.59	30	8.10 ± 0.46	-	3.24 ± 0.13
		30	42.26 ± 1.04		7.93 ± 0.34	-	2.90 ± 0.14
		60	44.53 ± 0.51		6.86 ± 0.73	-	2.82 ± 0.06
		90	46.51 ± 0.6		6.81 ± 0.46	-	2.88 ± 0.15
mean ±s.d.			**43.48 ±2.58**		**7.43 ±0.79**	-	**2.96 ±0.21**
G_n	4	0	50.79 ± 2.63	30	12.90 ± 0.78	2.08 ± 0.66	2.46 ± 0.18
	5	30	49.94 ± 6.04		11.67 ± 1.92	2.87 ± 0.37	2.58 ± 1.00
		60	51.17 ± 2.75		10.46 ± 1.18	2.25 ± 0.42	2.87 ± 0.39
		90	53.89 ± 4.04		11.36 ± 0.47	1.87 ± 0.60	1.74 ± 0.55
mean ±s.d.			**51.48 ±4.43**		**11.36 ±1.37**	**2.28 ±0.64**	**2.41 ±0.76**

fied by means of digital images that had been recorded previously. The strips were then fixed in clamps covered with sandpaper to reduce tissue slippage, see (d). The axial tension experiments were performed at a nominal strain rate of $\dot{\varepsilon} = 0.5\%$ s^{-1} up to failure of the strips without any preconditioning of the tissue. While the global displacement u of the upper clamp was specified by the testing machine, the resulting force F was measured and converted to mean engineering stress as $P = F/A$ by division through the un-deformed cross-sectional area A. The axial stretch $\lambda = 1 + u/l_0$, to be a global stretch measure, was calculated from u and the unde-formed sample length l_0, cf. Fig. 2 (d). All experiments were per-formed at room temperature within 5 h after organ removal.

2.5. Data processing

The experimental raw data in form of force and displacement include high numbers of measuring points, see supplementay data in Section. To make the data manageable all raw data underwent three processing steps: First, all data were smoothed and the num-ber of data point was reduced to a maximum of approximately 150. Secondly, the reference state was associated with a small pre-force of 30 mN, corresponding to about 1.4 kPa pre-stress. Note that the pre-loads were subtracted from the stress when plot-ting the results unless stated otherwise. Finally, the elastic regions of the force-displacement curves of group G_u were determined by successively computing tangents $\mathcal{T}_i$ by finite differences at the points u_i, $i = 1, 2, ..., m$, where m indicates the maximum number of measuring points. The elastic range of the curve is defined as the region where the slope is monotonically increasing, i.e., where $\mathcal{T}_{i+1} \geq \mathcal{T}_i$. The point u_j at which $\mathcal{T}_{j+1} < \mathcal{T}_j$ marks the end point of the elastic region. In a few cases this criterion was relaxed due to

the presence of very small drops in load within a region where the slope was still monotonically increasing. In such cases, these small drops were ignored for the purpose of defining the elastic region. Apart from this, measurements were discarded from the analyses if they could not be evaluated due to operational disturbances (e.g. slipping of the specimen or unintentional shift of the camera) and tearing of the specimens in the clamping region during tensile ex-periments.

3. Experimental results: direction-dependent force and stress responses

Fig. 3 (a) shows the results of the orientation-dependent ten-sion experiments of the un-notched samples (group G_u) in form of mean stress-stretch curves and standard deviation for the elas-tic region. Note that in order to provide mean values and standard deviations from all samples, the stretch range shown in Fig. 3 (a) corresponds to the smallest elastic region of the tested samples. Independent of the sample orientation all curves are characterized by a clearly nonlinear, exponential material response. The lowest stiffness is provided by those tissue samples, that are oriented par-allel (0°) to the circumferential SI axis, cf. Fig. 2 (b). With increas-ing sample orientation (30°, 60°, 90°) also the material stiffness increases, which indicates a strongly anisotropic material behavior. Table 2 shows the maximum stresses and stretches in the form of mean values and standard deviations. The lowest maximum stress is found in specimens aligned in the circumferential direction (0°). As the number of degrees increases, the maximum stresses also increase, while the maximum stretches decrease. Also with respect to Fig. 3 (a), the stretches indicating the end points of the elas-tic regions reduce from 1.96 (0°) over 1.74 (30°) and 1.49 (60°)
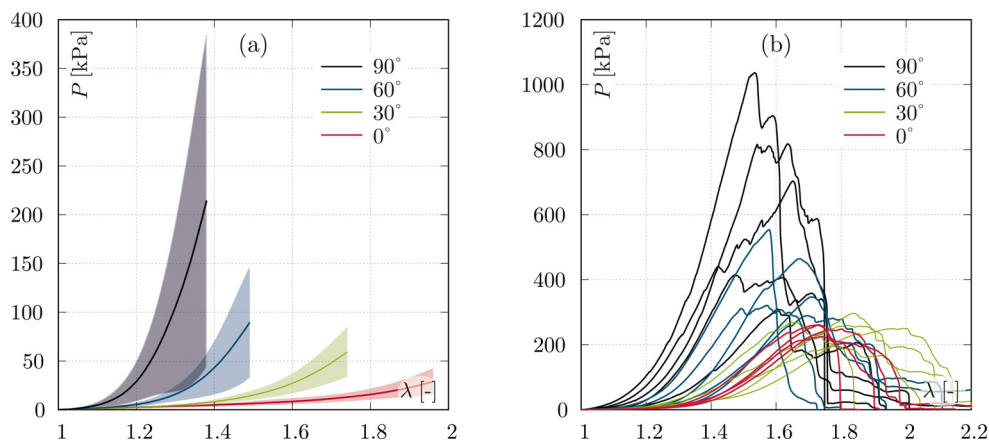
Fig. 3. Tensile stress-stretch responses of (a) un-notched and (b) notched SI samples. Solid curves indicate mean values whereas shaded areas depict the standard deviations.

Table 2
Mean and standard deviation of maximum stress P_{max} and λ_{max}. Note, the index 'max' indicated the end value of the material responses' elastic range.

	0°	30°	60°	90°
P_{max} [kPa]	95.2 ± 42.2	115.7 ± 31.8	117.3 ± 55.9	388.2 ± 118.3
λ_{max} [-]	2.3 ± 0.2	1.9 ± 0.2	1.6 ± 0.1	1.5 ± 0.1

to 1.38 (90°), while the stresses increase (29.0 kPa (0°), 59.1 kPa (30°), 89.1 kPa (60°), 213.9 kPa (90°)). In Fig. 3 (b) the results of the orientation-dependent tension experiments of the notched samples (group G_n) is shown. Compared to the un-notched samples, the 90° samples feature the stiffest material response followed by the 60° samples. The 30° and 0° samples, however, show similar mechanical characteristics.

4. Continuum mechanical model including fracture

The layered structure of the SI requires a model that takes into account the contributions of the individual layers. Here, we consider the three main layers (mucosal, submucosal, and muscular layer) responsible for the overall mechanical response of the tissue. While the mucosal layer can be considered isotropic and thus represents the isotropic ground matrix, the submucosal and muscular layers, which consist of fibers with preferred orientation, are anisotropic from a mechanical point of view. In the submucosal layer, the two sets of diagonally inclined collagen fibers include anisotropy. The stratum circulare and stratum longitudinale, which contain circular and longitudinal smooth muscle fibers, respectively, together form the anisotropic muscle layer, for more microstructural details see Section 2.2.

In the present work, the SI is treated as an incompressible and hyperelastic anisotropic material undergoing large deformation in a quasi-static setting. The material is assumed to be homogeneous whilst contributions from different layers are considered. The simplified material with the uniform distribution of different fibers in the isotropic base matrix, as shown in Fig. 4, models the layered structure of SI. With these assumptions, we adapt the HGO model in our study. Accordingly, the strain energy function is decomposed into two parts: A neo-Hookean component characterizing the isotropic ground matrix and the anisotropic four-fiber family containing longitudinal, circumferential, and diagonal fibers oriented at an angle α to the longitudinal direction as shown in Fig. 4, thus modeling the overall elastic response.
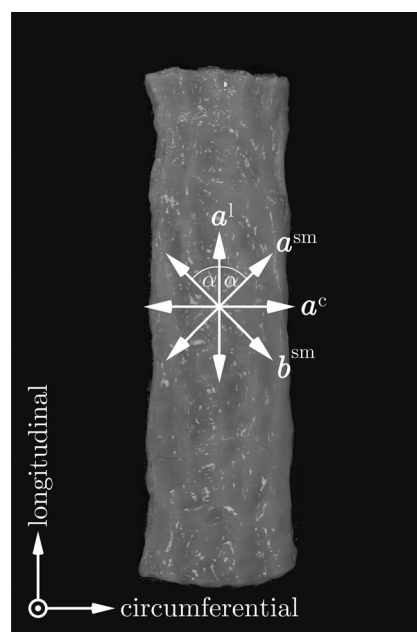

Fig. 4. Homogenized, single layer material consisting of isotropic ground matrix and a homogeneous distribution of fibers.

4.1. Continuum mechanical model

Based on general continuum mechanics, we consider an arbitrarily three-dimensional body represented by $\mathcal{B} \in \mathbb{R}^3$ in the reference configuration featuring the boundary $\partial\mathcal{B}$. Each material point $\boldsymbol{X} \in \mathcal{B}$ is mapped to its corresponding spatial point $\boldsymbol{x} \in \mathcal{S}$ by the nonlinear deformation map $\boldsymbol{\varphi}$ given by

$$\boldsymbol{x} = \boldsymbol{\varphi}(\boldsymbol{X}). \tag{1}$$

A map between the infinitesimal vector $d\boldsymbol{X}$ in the reference configuration and its spatial counterpart $d\boldsymbol{x}$ is due to the deformation gradient

$$\mathbf{F} = \frac{\partial \boldsymbol{x}}{\partial \boldsymbol{X}} = \nabla\boldsymbol{\varphi}, \tag{2}$$

where the operator ∇ denotes gradients with respect to the reference coordinates $\boldsymbol{X}$. Likewise, the infinitesimal volume elements are mapped from reference to spatial configuration via the Jacobian $J = \det(\mathbf{F}) > 0$. The symmetric right Cauchy-Green tensor

$$\mathbf{C} = \mathbf{F}^T\mathbf{F} \tag{3}$$

allows the determination of the invariants [98]

$$I_1 = \mathrm{tr}(\mathbf{C}),$$
$$I_2 = \frac{1}{2}\big[(\mathrm{tr}(\mathbf{C}))^2 - \mathrm{tr}(\mathbf{C}^2)\big], \quad \text{and}$$
$$I_3 = \det(\mathbf{C}). \tag{4}$$

Assuming a four-fiber family, we introduce four unit vectors $\boldsymbol{a}^{\mathrm{sm}}$, $\boldsymbol{b}^{\mathrm{sm}}$, $\boldsymbol{a}^{\mathrm{l}}$, and $\boldsymbol{a}^{\mathrm{c}}$, representing the two submucosal collagen fibers also referred to as diagonal fibers, the longitudinal and the circumferential fibers of the muscular layer, respectively, see Fig. 4. With the unit vectors at hand, the corresponding structural tensors read

$$\mathbf{M}^{\mathrm{sm},\boldsymbol{a}} = \boldsymbol{a}^{\mathrm{sm}} \otimes \boldsymbol{a}^{\mathrm{sm}},$$
$$\mathbf{M}^{\mathrm{sm},\boldsymbol{b}} = \boldsymbol{b}^{\mathrm{sm}} \otimes \boldsymbol{b}^{\mathrm{sm}},$$
$$\mathbf{M}^{\mathrm{l}} = \boldsymbol{a}^{\mathrm{l}} \otimes \boldsymbol{a}^{\mathrm{l}}, \quad \text{and}$$
$$\mathbf{M}^{\mathrm{c}} = \boldsymbol{a}^{\mathrm{c}} \otimes \boldsymbol{a}^{\mathrm{c}}. \tag{5}$$

Additionally, invariants necessary for the description of the anisotropic response of the tissue are defined as

$$I_4^{\mathrm{sm},\boldsymbol{a}} = \mathbf{C} : \mathbf{M}^{\mathrm{sm},\boldsymbol{a}},$$
$$I_6^{\mathrm{sm},\boldsymbol{b}} = \mathbf{C} : \mathbf{M}^{\mathrm{sm},\boldsymbol{b}},$$
$$I_4^{\mathrm{l}} = \mathbf{C} : \mathbf{M}^{\mathrm{l}}, \quad \text{and}$$
$$I_4^{\mathrm{c}} = \mathbf{C} : \mathbf{M}^{\mathrm{c}}. \tag{6}$$

To represent the global elastic response of SI tissues, the invariant-based total elastic strain energy function

$$\psi_{\mathrm{e}} = \psi_{\mathrm{e}}^{\mathrm{iso}} + \psi_{\mathrm{e}}^{\mathrm{ani}} \tag{7}$$

is additively decomposed into an isotropic ($\psi_{\mathrm{e}}^{\mathrm{iso}}$) and anisotropic ($\psi_{\mathrm{e}}^{\mathrm{ani}}$) part. The isotropic part

$$\psi_{\mathrm{e}}^{\mathrm{iso}} = \frac{\mu}{2}(I_1 - 2\ln J - 3) + \kappa(J - \ln J - 1), \tag{8}$$

modeled by a neo-Hookean hyperelastic formulation [40], characterizes the energy stored in the ground biological matrix. Herein, κ and μ are the bulk and shear moduli, respectively. The anisotropic component

$$\psi_{\mathrm{e}}^{\mathrm{ani}} = \psi_{\mathrm{e}}^{\mathrm{sm},\boldsymbol{a}} + \psi_{\mathrm{e}}^{\mathrm{sm},\boldsymbol{b}} + \psi_{\mathrm{e}}^{\mathrm{l}} + \psi_{\mathrm{e}}^{\mathrm{c}} \tag{9}$$

further comprises four terms

$$\psi_{\mathrm{e}}^{\mathrm{sm},\boldsymbol{a}} = \frac{k_1^{\mathrm{sm}}}{2k_2^{\mathrm{sm}}}\left\{ \exp\left[k_2^{\mathrm{sm}}\left(I_4^{\mathrm{sm},\boldsymbol{a}} - 1\right)^2\right] - 1 \right\},$$
$$\psi_{\mathrm{e}}^{\mathrm{sm},\boldsymbol{b}} = \frac{k_1^{\mathrm{sm}}}{2k_2^{\mathrm{sm}}}\left\{ \exp\left[k_2^{\mathrm{sm}}\left(I_6^{\mathrm{sm},\boldsymbol{b}} - 1\right)^2\right] - 1 \right\},$$
$$\psi_{\mathrm{e}}^{\mathrm{l}} = \frac{k_1^{\mathrm{l}}}{2k_2^{\mathrm{l}}}\left\{ \exp\left[k_2^{\mathrm{l}}\left(I_4^{\mathrm{l}} - 1\right)^2\right] - 1 \right\}, \quad \text{and}$$
$$\psi_{\mathrm{e}}^{\mathrm{c}} = \frac{k_1^{\mathrm{c}}}{2k_2^{\mathrm{c}}}\left\{ \exp\left[k_2^{\mathrm{c}}\left(I_4^{\mathrm{c}} - 1\right)^2\right] - 1 \right\} \tag{10}$$

of the individual fiber contributions in the submucosal (Eq. (10)$_{1,2}$), the stratum longitudinale (Eq. (10)$_3$), and in the stratum circulare Eq. (10)$_4$). Herein, $k_1^{\mathrm{i}} > 0$, $\mathrm{i} = \{\mathrm{sm}, \mathrm{l}, \mathrm{c}\}$, are material parameters related to the fiber stiffness with the units of stress and $k_2^{\mathrm{i}} > 0$ are dimensionless parameters quantifying the stiffening effect of the fibers with the deformation, see Holzapfel et al.[50]. Following Holzapfel [49], the fibers are considered in case of tensile loading while they do not contribute to compressive loads.
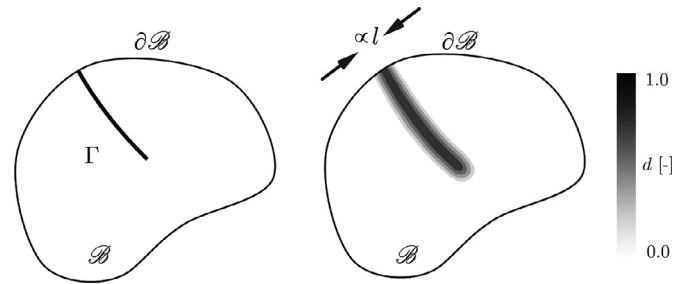

Fig. 5. Phase-field modeling of a crack in a body $\mathcal{B}$: (a) Sharp crack topology and (b) regularized crack.

Finally, the second Piola-Kirchhoff stress tensor

$$\begin{aligned}
\mathbf{S} &= \mathbf{F}^{-1}\frac{\partial \psi_{\mathrm{e}}(\mathbf{F})}{\partial \mathbf{F}} \\
&= \kappa(J-1)\mathbf{C}^{-1} + \mu(\mathbf{I} - \mathbf{C}^{-1}) \\
&\quad + 2k_1^{\mathrm{sm}}\Big[(I_4^{\mathrm{sm},\boldsymbol{a}} - 1)\exp\left[k_2^{\mathrm{sm}}(I_4^{\mathrm{sm},\boldsymbol{a}} - 1)^2\right]\mathbf{M}^{\mathrm{sm},\boldsymbol{a}} \\
&\quad + (I_6^{\mathrm{sm},\boldsymbol{a}} - 1)\exp\left[k_2^{\mathrm{sm}}(I_6^{\mathrm{sm},\boldsymbol{b}} - 1)^2\right]\mathbf{M}^{\mathrm{sm},\boldsymbol{b}}\Big] \\
&\quad + 2k_1^{\mathrm{l}}(I_4^{\mathrm{l}} - 1)\exp\left[k_2^{\mathrm{l}}(I_4^{\mathrm{l}} - 1)^2\right]\mathbf{M}^{\mathrm{l}} \\
&\quad + 2k_1^{\mathrm{c}}(I_4^{\mathrm{c}} - 1)\exp\left[k_2^{\mathrm{c}}(I_4^{\mathrm{c}} - 1)^2\right]\mathbf{M}^{\mathrm{c}}
\end{aligned} \tag{11}$$

can be straightforwardly determined.

4.2. Phase-field description of fracture

In this section, we firstly present the basic phase-field fracture model considering an isotropic material to highlight the key ingredients of the approach in the simplest setting. Departing from this model, we then present an extension of the same to the anisotropic SI tissue. The extended model coupled with finite elasticity introduced in Section 4.1 thus incorporates anisotropy of SI both in the elastic and fracture energy densities.

Suppose that the domain $\mathcal{B}$ contains a sharp crack Γ as shown in Fig. 5 (a). The energy associated with the fracture surface is

$$\mathcal{E}_\Gamma = \int_\Gamma G_{\mathrm{c}} \, d\Gamma, \tag{12}$$

where $G_{\mathrm{c}} > 0$ is the fracture toughness of the material. Within the phase-field framework, the discrete crack Γ is approximated by the steep local variation of a continuous scalar field variable called the *phase-field* d varying between 0 and 1 at intact material points and a fully damaged region, respectively, see also Fig. 5 (b). This transition from undamaged to damaged region occurs over a zone whose size is controlled by the *length-scale* parameter l leading to a diffused crack. After the regularization introduced by the phase-field model, the surface integral in Eq. (12) is approximated by a volume integral

$$\mathcal{E}_\Gamma \approx \int_\mathcal{B} G_{\mathrm{c}}\psi_f(d) \, d\mathcal{B} = \int_\mathcal{B} \frac{G_{\mathrm{c}}}{c_w}\left[\frac{w(d)}{l} + l\nabla d \cdot \nabla d\right]d\mathcal{B}, \tag{13}$$

where the *dissipation function* $w(d)$ controls the decaying profile of d and c_w is an associated normalization constant. Two widely adopted choices include $w(d) = d$ and d^2 for which $c_w = 8/3$ and 2, respectively. The linear dissipation function model is commonly referred to as the AT-1 model, while the latter choice leads to the AT-2 model, where AT stands for Ambrosio-Tortorelli [3]. The main difference between the two choices is the existence of a purely elastic phase before the onset of phase-field crack evolution in case of AT-1. In this work, we study the fracture behavior of SI using both the models.

Phase-field models converge (in the Γ-convergence sense) to the variational formulation of brittle fracture [31] as l tends to zero
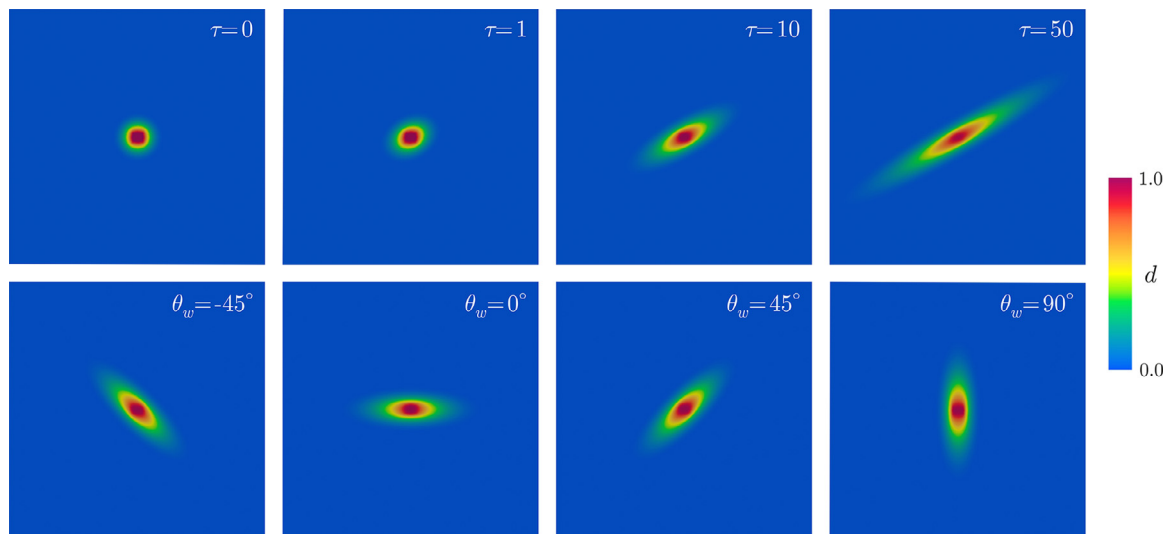
Fig. 6. Parametric study on anisotropic phase-field regularization for a pre-existing crack using the AT-1 model. Varying τ at $\theta_w = 30°$ (first line) and varying θ_w at $\tau = 10$ (second line).

[11,12]. Such regularization eliminates the inherent discontinuities in the displacement field at the locations of the crack. Evolution of the phase-field variable based on energy minimization principle governs the process of crack propagation. This eliminates the tedious task of algorithmic crack tracking, which is especially laborious in scenarios with complex crack patterns, crack fusion or branching, and in three dimensions. The non-local nature of the model eliminates mesh dependence, a major drawback of local damage models [4,57]. Additionally, flexibility in this framework provides a suitable platform for its extensions to several problems, including failure in soft biological tissues exhibiting anisotropy in fracture properties.

The individual components constituting the tissue, namely the four fiber families and the ground matrix, have distinct fracture toughness values. Thus, the resulting homogenized material exhibits fracture anisotropy. This means that the fracture toughness is no longer a constant but direction dependent. In order to determine the exact contour of the anisotropy, it is necessary to study the fracture in the individual tissue layers subjected to different mechanical loading, in addition to the overall mechanical response of the tissue. Based on the found experimental evidences for crack propagation path and literature on the topic [41,42], we assume a two-fold symmetric fracture anisotropy in the present study. Accordingly, Eq. (13) can be rewritten as

$$\mathcal{E}_\Gamma^{\text{ani}} = \int_\Gamma G_c(\boldsymbol{n})\, d\Gamma \approx \int_{\mathcal{B}} \frac{G_c}{c_w} \left[\frac{w(d)}{l} + l\nabla d \cdot \mathbf{A}\nabla d \right] d\mathcal{B}. \tag{14}$$

Herein, $\boldsymbol{n}$ is a unit normal vector to the surface and the dependence of G_c on it indicates direction dependence of fracture toughness. The same is incorporated within the phase-field model by the introduction of a structural tensor

$$\mathbf{A} = \mathbf{I} + \tau\,(\boldsymbol{a} \otimes \boldsymbol{a}) \tag{15}$$

in the non-local part of the fracture energy as indicated in Eq. (14), see also Teichtmeister et al. [102]. Herein, $\tau \in [-1, \infty]$ is the so-called anisotropy parameter controlling the extent of anisotropy along a given weak direction $\boldsymbol{a}$ oriented at an angle θ_w with respect to the horizontal axis. The above form of the structural tensor achieves the required two-fold symmetry of the fracture toughness. The parametric influence of θ_w and τ is depicted in Fig. 6, where plots of phase-field regularization for a pre-existing central crack in a square domain are shown. It should be noted that setting the anisotropy parameter $\tau = 0$ recovers the isotropic case.

The total free energy of the system can be now expressed as

$$\mathcal{E}_l(\mathbf{F}, d) = \int_{\mathcal{B}} \left(g(d)\psi_e(\mathbf{F}) + \frac{G_c}{c_w}\left[\frac{w(d)}{l} + l\nabla d \cdot \mathbf{A}\nabla d \right] \right) d\mathcal{B}, \tag{16}$$

to be the sum of elastic in Eq. (7) and fracture contributions in Eq. (14). Here, the *degradation function* $g(d)$ couples the elasticity and phase-field problems and ensures a decrease in elastic stiffness properties with crack growth. In the present work, we choose the quadratic degradation function $g(d) = [(1-d)^2 + \eta]$. The dimensionless parameter η, set to 10^{-5}, represents artificial residual stiffness in a fully broken material as the phase-field reaches unity and is used for numerical stability reasons. Minimization of the total free energy in Eq. (16) leads to the coupled Euler-Lagrange governing equations

$$\text{Div}\big[g(d)\mathbf{FS}\big] = 0 \quad \text{on} \ \mathcal{B} \tag{17}$$

$$g'(d)\mathcal{H} - \frac{G_c}{c_w}\left[\frac{w'(d)}{l} - 2l\,\text{Div}(\mathbf{A}\nabla d) \right] = 0 \quad \text{on} \ \mathcal{B} \tag{18}$$

in the reference coordinates, where, following Miehe et al. [67], a history variable

$$\mathcal{H} = \max_{s\in[0,t]} \ \psi_e(\mathbf{F}, s) \tag{19}$$

is introduced, wherein t represents a pseudo-time, to impede healing of cracked material points thus enforcing crack irreversibility (see Gerasimov and de Lorenzis [37] for other crack irreversibility enforcing techniques).

Finally, Dirichlet and Neumann boundary conditions for deformation maps applied on $\partial\mathcal{B}_\varphi$ and $\partial\mathcal{B}_T$, respectively ($\partial\mathcal{B}_\varphi \cup \partial\mathcal{B}_T = \partial\mathcal{B}$, $\partial\mathcal{B}_\varphi \cap \partial\mathcal{B}_T = \emptyset$), along with the natural boundary condition for the phase-field

$$\boldsymbol{\varphi} = \bar{\boldsymbol{\varphi}} \quad \text{on} \ \partial\mathcal{B}_\varphi \tag{20}$$

$$\mathbf{FS} \cdot \boldsymbol{N} = \bar{\mathbf{T}} \quad \text{on} \ \partial\mathcal{B}_T \tag{21}$$

$$[\mathbf{A}\nabla d] \cdot \boldsymbol{N} = 0 \quad \text{on} \ \partial\mathcal{B} \tag{22}$$

complete the boundary value problem which models anisotropic coupled hyperelasticity and fracture in SI tissues.

5. Results

In this section, the numerical results obtained by the finite element analysis of intestinal tissue strips using the continuum mechanical model discussed in the previous section are presented. Firstly, a constitutive material parameter evaluation procedure based on experimental data obtained from tension tests is discussed. Then, notched tissue strips subjected to uniaxial tension are considered to simulate tissue failure. Introduction of a notch results in controlled fracture leading to crack propagation originating from the notch without which the specimens would mostly fail at the boundaries where they are gripped. Such a response is finally simulated using the phase-field model discussed in Section 4.2. Results obtained using both AT-1 and AT-2 formulations are presented.

5.1. Calibration of elastic constitutive parameters

The constitutive parameters $\mu, \kappa, k_1^{sm}, k_2^{sm}, k_1^l, k_2^l, k_1^c, k_2^c, \alpha$ appearing in the modeling approach, presented in Section 4.1, are to be calibrated. Herein, α represents the orientation of the diagonal or submucosal fibers with respect to the longitudinal direction as indicated in Fig. 4. Due to the assumed incompressibility of the material, κ acts as a penalty parameter whose value is set a priori to 50 kPa, since the results remain unchanged at a higher penalty value of 100 kPa. Hence, a total of eight parameters ($n_p = 8$) are to be calibrated using the elastic region of the experimental curves. To this end, the experimental, orientation dependent ($\theta \in D = \{0°, 30°, 60°, 90°\}$) stress-stretch relationships, as shown in Fig. 3 (a), are used.

Calibration is performed using a least-squares type analysis where the objective function

$$\mathcal{O} = \sum_{\theta \in D} \sum_{j=1}^{n_\theta} (P_{\theta,j}^{exp} - P_{\theta,j}^{num})^2, \tag{23}$$

containing the sum of squared residuals between experimentally ($P_{\theta,j}^{exp}$) and numerically ($P_{\theta,j}^{num}$) obtained first Piola-Kirchhoff stresses is minimized using the in-built function *lsqonlin* in MATLAB®, for enhanced deterministic-stochastic optimization algorithms [72,110]. Note that, in order to satisfy thermodynamics requirements, suitable ranges to the values of the material parameters and of the tangent material parameters may need to be enforced, see e.g. Scott [89] for the simpler case of isotropic hyperelasticity. The obtainment of corresponding bounds for the anisotropic material model at hand would be worthy of investigation but is postponed to further research. However, we enforce the positivity constraint for k_1^i and k_2^i as mentioned in Holzapfel et al. [50] by setting a zero lower limit for these parameters in our minimization. Also, following the limits established using scanning electron microscopy for rat SI in Komuro [56] and with additional relaxation to the same, we prescribe physically realistic limits of $\{25°, 60°\}$ for α.

In Eq. (23), n_θ defines the number of data points for each $\theta \in D$. Two experimental data sets representing the maximum and minimum limits for each θ are identified. The calibration procedure is performed for the two data sets individually. Instead of a single set of mean curves, two sets of data are identified since the experimental data showed a distribution with a moderately high standard deviation for each θ. Such a calibration procedure will thus result in a range of estimated values that a parameter could assume for the material under consideration. For the realization of the numerical analyses, a finite element mesh, featuring approximately 4500 eight-noded three-dimensional brick elements, was used. According to the experimental setup illustrated in Fig. 2 (d),

one end on the specimen was fixed, while the other one was subjected to displacement controlled loading.

In Fig. 7 (a) and (b) the upper and lower bound of the orientation dependent stress-stretch relations in form of the numerical results versus the experimental ones are illustrated. The agreement between the experimental and numerical results is very good. This is also evident from the corresponding root mean square error values in Table 3, which were calculated as

$$\varepsilon = \sqrt{\frac{\mathcal{O}_{min}}{\sum_{\theta \in D} n_\theta - n_p}}. \tag{24}$$

Calibration of the parameters using maximum and minimum data sets yields a range for the parameters that results in an envelope of mechanical responses that can be captured by the model, as shown in Fig. 7 (c). The corresponding values obtained for the elastic parameters are given in Table 3. To try to approach as closely as possible the absolute minimum, we carried out the minimization process for different initial guesses until similar results with multiple initial guesses were obtained and these results led to a reasonable value of the cost function, hence a sufficiently close fit. However, a possible better way of proceeding may involve e.g. randomly chosen initial guesses, leading to a probability distribution for the solution of the minimization procedure and thus to multiple local minima with corresponding probabilities. Such a procedure would also allow identifying possible multimodal behavior of the cost function.

Finally, in Fig. 8 the Cauchy stress distribution in axial direction of the specimen is shown. These plots in the deformed configuration reveal that the configuration in which the specimen is loaded along the circumferential direction ($\theta = 0°$) undergoes the maximum deformation, while this maximum deformation decreases with increasing θ. This is in line with the experimental observation discussed in Section 3.

Remark 1 (Calibration with a modified constraint). During the above calibration procedure, we encountered unphysically high values of lateral strains (over all cases of θ) when the minimization was enforced only with the positivity constraint for μ. The reason was the extremely low values of μ, leading to such undesirable effects. Therefore, a lower bound of 2.5 kPa was introduced for μ, based on the experimentally observed transverse strain values, in order to obtain physically reasonable transverse strain quantities.

5.2. Calibration of phase-field fracture parameters

For the numerical study of the fracture behavior of SI tissue, we make use of the experimental data obtained from tests on notched samples (group G_n) presented in Section 3, see Fig. 3 (b). Similar to the previous study, for each $\theta \in D = \{0°, 30°, 60°, 90°\}$, a maximum and a minimum data set are identified and are used in the subsequent numerical analysis. The numerical investigation of the experimentally observed fracture behavior is carried out in the framework of the anisotropic phase-field model discussed in Section 4.2. This introduces three additional parameters, namely, the fracture toughness G_c, the anisotropy parameter τ, and the weak direction θ_w, which needs to be calibrated. While G_c and τ strongly affect the peak load at which crack propagation begins, the crack propagation direction is guided by θ_w and τ. For this reason, a two-step analysis methodology is presented: First, the calibration of the eight elastic constitutive parameters is performed using the experimental stress-stretch data before the onset of fracture with the procedure described previously, see Section 5.2, while the value of the fracture toughness is estimated simultaneously. In the second step, using the calibrated elastic constitutive parameters and the approximate estimate for G_c as initial values, we calibrate the three
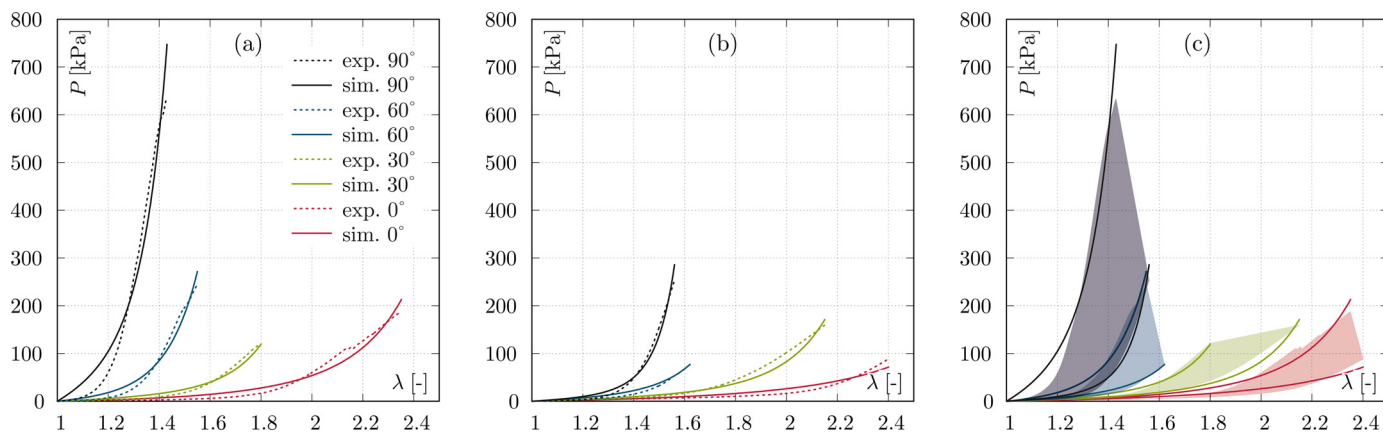
Fig. 7. Uniaxial tension test on un-notched specimen. Comparison of numerically obtained stress-stretch responses (solid lines) to the corresponding experimental curves (dotted lines) for (a) maximum and (b) minimum limits of the experimental data. (c) Combined response, solid lines depict numerical results and the shaded area represents the envelope within which the experimentally obtained responses lie.

Table 3
Identified material parameters using the experimental maximum and minimum data sets of the un-notched specimens.

border	μ [kPa]	k_1^{sm} [kPa]	k_2^{sm} [-]	k_1^{l} [kPa]	k_2^{l} [-]	k_1^{c} [kPa]	k_2^{c} [-]	α [°]	ε [kPa]
maximum	2.50	7.38	0.60	77.35	1.04	0.95	0.06	39.78	16.71
minimum	2.50	3.65	0.31	5.14	1.19	0.78	0.02	38.16	10.56

parameters of the phase-field model using the experimentally obtained peak stresses in an analogous minimization procedure as in the previous step. This calibration procedure is carried out individually using both AT-1 and AT-2 anisotropic phase-field models. The bounds for θ_w needed for the calibration procedure are estimated from the experimentally observed crack histories as $\{-10°, 10°\}$.

The problem setup for the phase-field fracture study employing the finite element analysis remains the same as in the previous section except that a pre-existing cut as indicated in Fig. 2 (c) needs to be additionally introduced. Similar to Borden et al. [9], the initial notch in the specimen is defined in the numerical analysis using the history variable $\mathcal{H}$ in Eq. (19), see Fig. 9.

The domain is discretized with 8400 eight-noded three-dimensional brick elements, and the length scale parameter associated with the width of the diffuse crack approximation is set to a relatively small value of 0.5 mm compared to the dimensions of the sample. The coupled elasticity and phase-field equations are solved using a staggered procedure in which the mechanical and phase-field subproblems are solved independently, alternating until convergence [67].

Remark 2 (Material parameter interpretation of the length-scale parameter). In our treatment, the length-scale parameter appearing in the phase-field model is purely a numerical quantity that controls the width of the phase-field crack and has no physical meaning associated to it. It is hence pre-determined and set to a constant value. In many phase-field fracture studies [9,82,101,109], the length-scale parameter is considered a physically meaningful material parameter that controls the stress at which a crack nucleates in the domain. Since our study focuses on a sample with a pre-existing singularity, it is sufficient to take a predefined value of the length scale, as this does not significantly affect the results in such cases, see Tanné et al. [101].

The numerically obtained stress-stretch curves for the corresponding maximum and minimum experimental data sets, using the two-step calibration procedure explained above, are shown in Fig. 10 (a) and (b), respectively.

Herein, results using both formulations (AT-1 and AT-2) can be seen in comparison with the experimental curves. As can be seen, a good agreement between the experimental and numerical response can be observed in the results of both the AT-1 and AT-2 models. This close agreement is obtained not only in the elastic region but also in the peak stresses. In each case, the nonlinear progression in the elastic region followed by a drop in stress values due to the onset of crack propagation is well captured.

The corresponding values obtained for the elastic constitutive parameters and the phase-field parameters are presented in Table 4. The calibrated elastic parameters using AT-1 and AT-2 models do not exactly coincide for the reason that unlike the AT-1 model, phase-field starts evolving from the very beginning of loading in the AT-2 model, thus leading to a slightly different elastic response. However, in many cases, the corresponding calibrated parameter values using the two are in close comparison to each other.

Finally, Fig. 11 compares the numerically obtained phase-field crack paths to the corresponding experimental crack paths. While the phase-field parameter reaches 1 within the transition zone when the same remains close to 0 elsewhere in case of the AT-1 phase-field model, results using the AT-2 model is damage-like with non-zero phase-field values away from the crack. Nevertheless, in both cases the experimentally revealed fracture anisotropy of the intestinal tissue is well-replicated where we observe the variation of the crack propagation path with the loading direction. For $\theta = 0°$, the crack propagates at a small angle to the longitudinal fiber oriented along the $\boldsymbol{e}_1$-direction, and the same increases with θ. However, the weak direction remains close to the longitudinal direction for all θ as indicated by the values of θ_w in Table 4.

Remark 3 (Need for operator intervention in calibration of the phase-field parameters). In calibrating the phase-field fracture parameters, we encountered scenarios where minimization resulting from a straightforward adoption of the optimization algorithm for certain parameter values resulted in crack propagation at domain boundaries. This led to the need for some manual intervention in
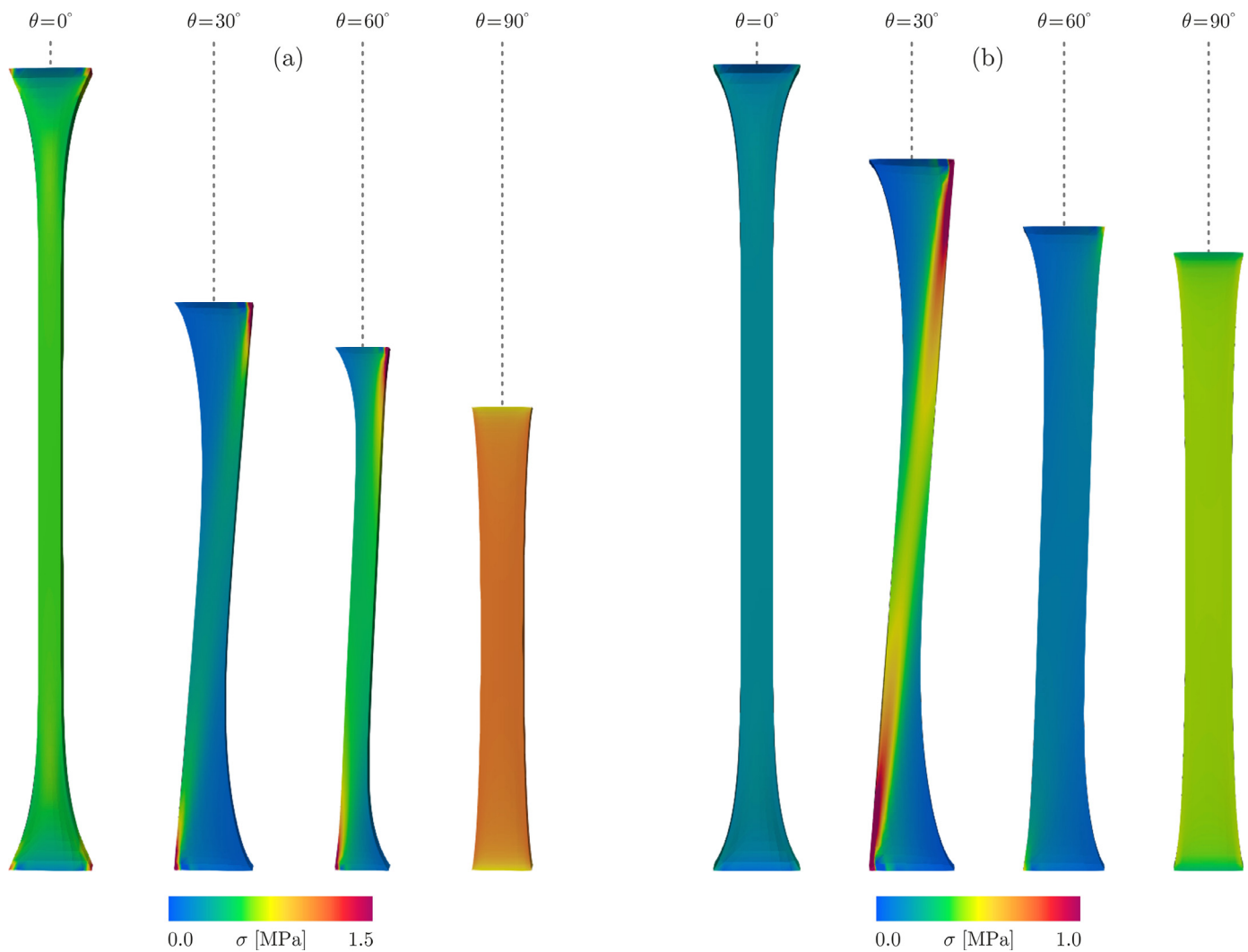
Fig. 8. Uniaxial tension test on un-notched specimen: Contour plots of Cauchy stress σ along the longitudinal direction in MPa for (a) maximum and (b) minimum limits plotted on the deformed configuration.

Table 4
Identified material parameters (elastic and phase-field parameters) using the experimental maximum and minimum data sets of the notched specimens.

model	border	μ [kPa]	k_1^{sm} [kPa]	k_2^{sm} [-]	k_1^l [kPa]	k_2^l [-]	k_1^c [kPa]	k_2^c [-]	α [°]	G_c [N/m]	τ [-]	θ_w [°]
AT-1	maximum	5.01	38.43	1.13	32.23	1.21	19.52	0.37	30.10	0.28	60.11	5.49
	minimum	2.76	12.59	0.16	46.52	0.86	8.50	0.34	43.86	0.22	95.12	-8.10
AT-2	maximum	2.51	38.42	1.13	32.27	1.73	19.56	0.37	34.52	0.24	99.01	5.56
	minimum	2.50	9.47	0.65	27.66	2.18	10.10	0.58	41.86	0.13	90.44	-8.69

the minimization process, where we had to fine-tune the initial estimation of these parameters to ensure crack propagation from the first notch.

6. Discussion

6.1. Small intestine mechanical properties

Within this study, axial tension experiments were performed to identify the SI's orientation-dependent elastic and fracture mechanical characteristics, see Fig. 3. Overall, independent of the sample orientation, the SIW is characterized by clearly nonlinear material behavior, following clear exponential courses. With increasing orientation, the stiffness increases and the maximum elastic range decreases, see (a). The SI thus exhibits a strongly anisotropic material behavior. Previous studies on the mechanical properties of the SI show similar trends when realizing uniaxial tension experiments [27,46]. However, in none of these studies the mechanical behavior was systematically analyzed in terms sample orientation as it was done, e.g. for large intestine tissue [13–15]. Moreover, human cadaveric tissue [27], which makes a direct comparison with the results obtained in the present study impossible. Furthermore, even after intensive literature research, no experimental investigations could be found regarding the failure behavior of SI tissue, which once again emphasizes the uniqueness of the experimental data obtained here.
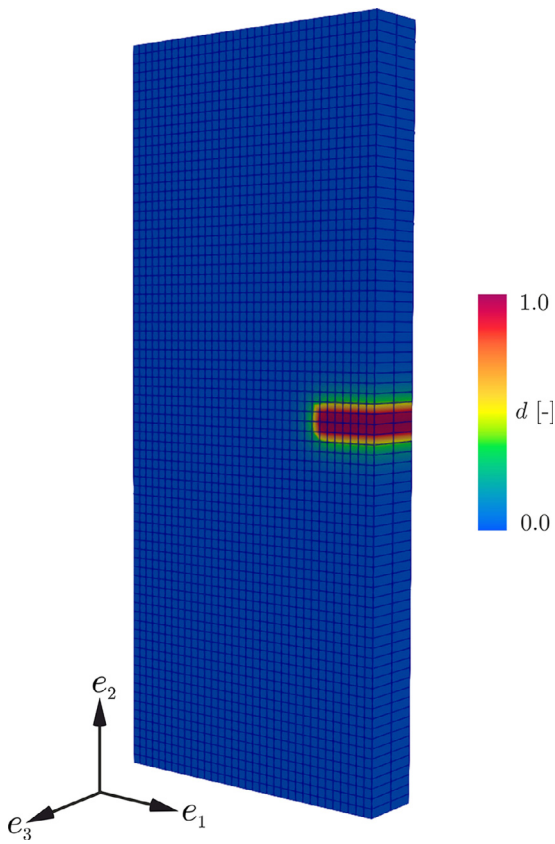
Fig. 9. Uniaxial tension test on notched specimen: Finite element mesh introduced with the initial phase-field edge notch.

6.2. Modeling the fracture behavior of the small intestine wall

The continuum mechanical model encompassing the layered structure of the SI coupled with the phase-field framework for fracture analysis presented in this work is a successful step towards modeling the anisotropic elastic and fracture behavior of the tissue. The close fit obtained for the nonlinear stress-stretch data confirm the construction of a neo-Hookean and the four-fiber family based strain energy density. The observed convergence of the

minimization problem for the calibration suggests that the constitutive description has not suffered over-parameterization. In the calibration of elastic constitutive parameters, smaller values obtained for k_1^c and k_2^c in comparison with other parameters indicate a relatively lower stress bearing capacity of the circumferential muscle layer. Among the remaining parameters, high values of k_1^l and k_2^l are obtained. This is supported by the large difference observed in the stiffness behavior of the two extreme loading angles $\theta = \{0°, 90°\}$ in Fig. 3 (a), where a stiffer behavior is observed in the latter case when the specimen is loaded along the longitudinal direction. A similar observation is also made in Sokolis [93] for rat SI and Patel et al. [80] in the context of swine colon. The calibrated range for the orientation of the diagonal fibers with respect to the longitudinal fibers $\alpha \in \pm[30.10°, 43.86°]$ (considering the fit for both notched and un-notched specimen data) agrees well with the experimentally found range $\pm[30°, 50°]$ in Komuro [56] for rat SI. On the other hand, our attempt to use the parameter values in Table 3 resulting from the calibration procedure for the un-notched samples as limits for calibrating the model parameters with the notched samples resulted in an insufficient fit with large mean square errors, necessitating the use of wider limits. The final numerical fit for the notched sample data, as shown in Table 4, has parameter values outside the expected range. A careful investigation by the comparison of the considered maximum and minimum experimental data sets for un-notched and notched specimens as shown in Fig. 12 reveal, contrary to the expectation, that the range of elastic response of the two tests do not coincide. The responses of the notched sample under extension (represented by the darker envelopes) are mostly outside the range of responses that can be captured by the calibrated parameters from the un-notched experimental data (represented by the lighter envelopes), justifying the observed discrepancy in the two sets of calibrated parameters. It is noted here that, contrary to the previous observation, the parameter values related to the circumferential fibers are no longer insignificant compared to those of the other fiber families. However, the observed stiffer behavior in the notched specimen response data, specifically in the case of $\theta = 0°$ and $\theta = 30°$, may have different reasons. In general, biological tissues show relatively large variations, which are due to e.g. animal husbandry, animal age, or general condition of the animal.

Mode I failure is a fracture mode in which the crack propagation occurs in a plane perpendicular to the tensile axis. The deviation of the crack propagation direction from this failure mode,
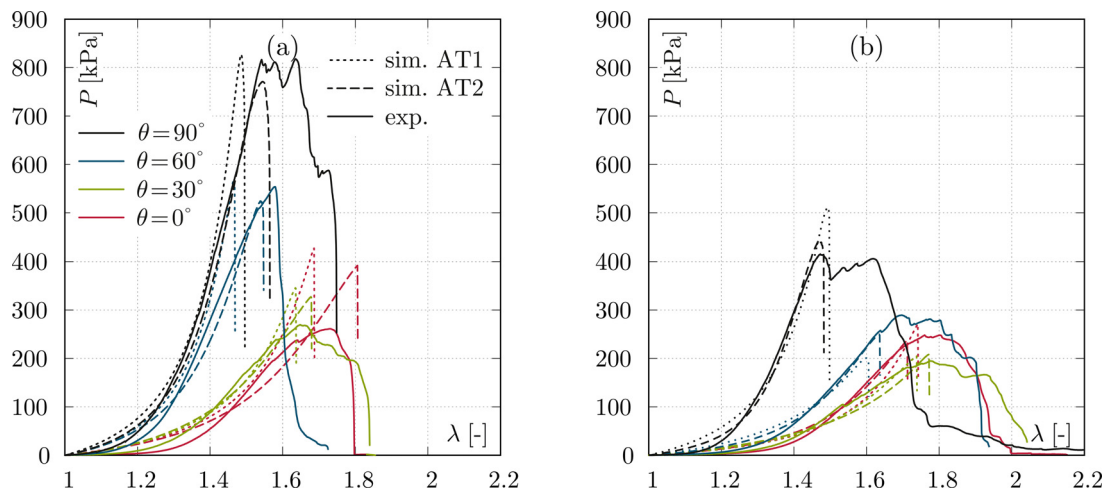

Fig. 10. Uniaxial tension test on notched specimens: Comparison of numerically obtained stress-stretch responses using AT-1 and AT-2 models to the corresponding experimental curves for (a) maximum and (b) minimum limits of the experimental data.
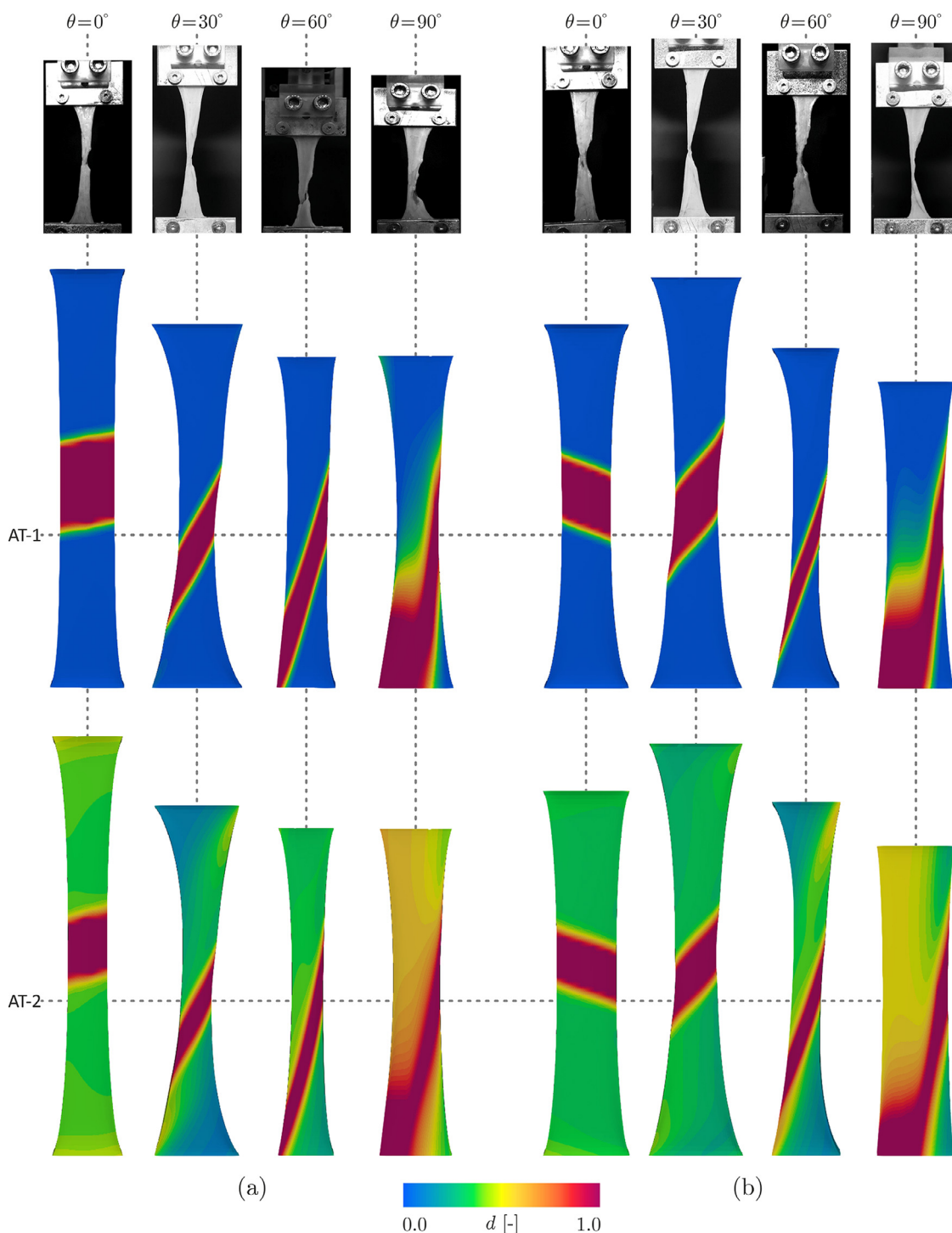
Fig. 11. Uniaxial tension test on notched specimens: Comparison of numerically obtained phase-field crack paths using AT-1 and AT-2 models to the experimentally observed crack paths for (a) maximum and (b) minimum limits of the experimental data.

which is the unique property of anisotropic failure is well-captured by the anisotropic phase-field model. The agreement of the numerical crack paths with their experimental counterparts in results of both AT-1 and AT-2 models advocate our earlier assumption of the two-fold symmetric fracture toughness for the overall fracture behavior of the considered tissue. In agreement with the experimental observations, the existence of a preferred direction along which the crack tends to propagate is clearly demonstrated in the phase-field simulations, with a high value of the anisotropy parameter,

as given in Table 4, supporting this claim. This weak direction, oriented at θ_w with respect to the longitudinal fiber, is in the range $[-8.10°, 5.49°]$ for AT-1 and $[-8.69°, 5.56°]$ in the case of the AT-2 formulation. The quantitative comparison of the peak stresses obtained in the phase-field simulation with the experimental data confirms the applicability of the phase-field model for predicting SI tissue failure. In this particular case, the absence of a purely elastic phase in the AT-2 model leads to a closer match of the stress-stretch response in the elastic region as well as the peak stress
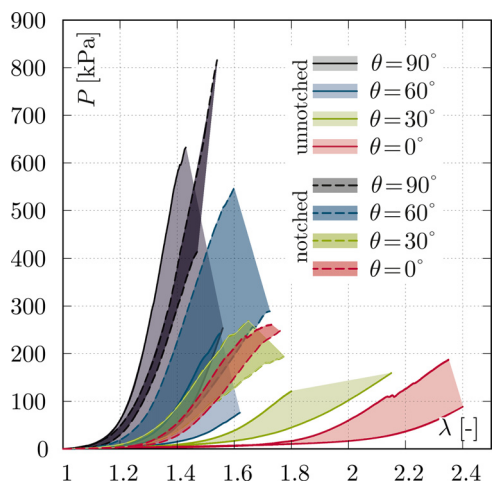
Fig. 12. Experimentally obtained envelope of elastic response for un-notched (lighter shade envelopes with solid lines) and notched (darker shade envelopes with dotted lines) specimens under uniaxial tension.

values with the experimental results, as shown in the combined maximum and minimum responses for AT-1 and AT-2 in Fig. 13 (a) and (b), respectively.

6.3. Limitations of the study

Despite the ability of the model to reproduce experimental results as evident in the numerical outcome, we need to acknowledge the shortcomings of the study. Layer-specific mechanical tests and failure analysis play an important role in gaining specific insights about the mechanical behavior of the individual constituents. Such a layer-specific calibration procedure enables blind predictions at the organ scale. In the present study, the calibration of elastic constitutive parameters in the model considering contributions from different layers to the strain energy density is done with the overall response data from the experiments which does not reveal layer-specific mechanical features. Secondly, in the study, six sets of elastic constitutive parameters, two sets corresponding to un-notched and two sets each using AT-1 and AT-2 models corresponding to notched experimental data, are obtained. Our attempt to evaluate the descriptive capability of the elastic parameters in Table 3 by applying them to describe the notched

group (G_n) of experimental data is inconclusive. Hence, evaluation of the predictive capabilities of the model and the task of choosing the most suitable set of parameters for SIs among the obtained remains an open issue and is to be addressed in future work. Layer-specific experimental details and analysing the not-connected regions of the parameters as suggested in Zanelli et al. [110] which sheds light on the relation between the uniqueness of model parameters and set of experiments would provide the necessary information to tackle this. Similarly, although the assumption of two-fold symmetry directed by the existence of one weak direction for fracture anisotropy of the overall tissue is determined to be plausible, layer-specific failure analysis is crucial since individual layers might exhibit anisotropy that is different from the overall two-fold symmetry. The overall anisotropy of fracture toughness would then be a superposition of the individual anisotropies. Not only does the resultant contour of fracture toughness model overall fracture with better accuracy, but is also an essential information required to capture delamination of individual layers. In this paper, we concentrate on quasi-static setting, neglecting strain-rate effects. Hysteresis, although shown to be negligible under certain loading rates for SI [77,92], should be considered for a complete analysis [16]. A visco-elastic framework including fracture for the analysis of failure in SI tissues will be addressed in our future studies. In the present study only purely passive properties are characterized. From a clinical point of view, however, it will be the case that even in the non-contracted state, the SI tissue will have an active force component. Thus, in future, appropriate failure experiments on active or partly active tissues will have to be performed and the present modelling approach will have to be extended accordingly. The framework presented here along with the above suggested extensions to incorporate more intricate details to accurately model the mechanical behavior of SI will result in a well-rounded tool necessary to understand the effects of GIPs. The continuum mechanical model including fracture provides a framework to model material degradation as the GIP progresses. The presence of a vulnerable direction for crack propagation as revealed in this study along with layer-specific fracture analysis would provide useful insights for attenuating the progression of GIPs. The knowledge about the mechanical and fracture behavior of individual constituents is thus crucial in building a comprehensive computational framework for failure analysis of intestinal tissues. This demands concentrated efforts from both experimental and modeling quarters and will be the focus of our future research.
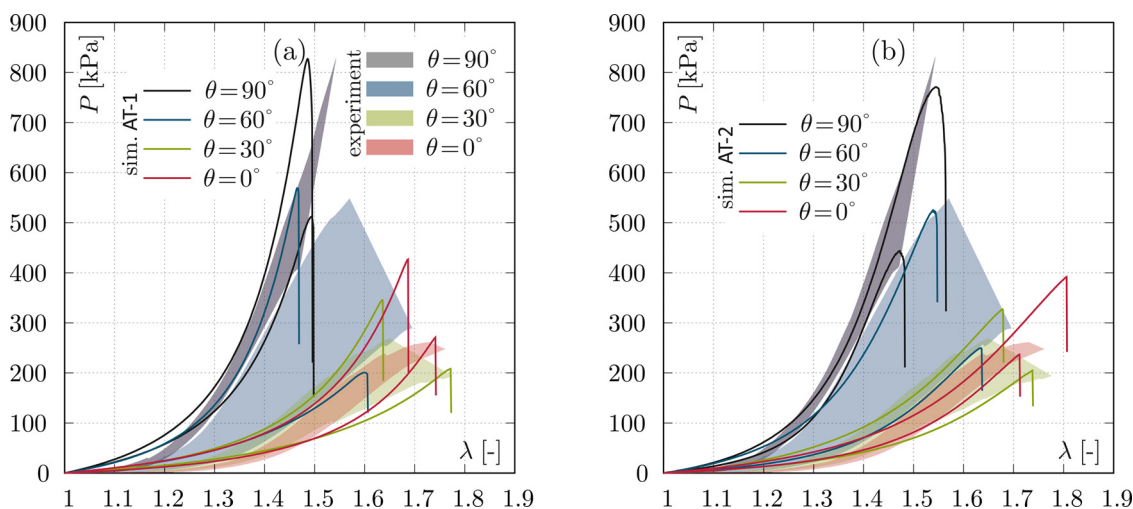

Fig. 13. Uniaxial tension test on notched specimens: Combined stress-stretch response where solid lines depict numerical results (upper and lower bounds) using (a) AT-1 and (b) AT-2 models and the shaded area represents the experimentally obtained envelope.

Declaration of Competing Interest

The authors declare that they have no known competing financial interests or personal relationships that could have appeared to influence the work reported in this paper.

Acknowledgements

Supplementary material

Supplementary material in form of unprocessed raw data (force-strain and stress-strain relations) of Fig. 3 can be found, in the online version, at doi:10.1016/j.actbio.2021.06.002.

References

[1] H. Ahmadzadeh, M.K. Rausch, J.D. Humphrey, Modeling lamellar disruption within the aortic wall using a particle-based approach, Sci. Rep. 9 (1) (2019) 15320.

[2] M. Ambati, T. Gerasimov, L. de Lorenzis, A review on phase-field models of brittle fracture and a new fast hybrid formulation, Computat. Mech. 55 (2) (2015) 383–405. ISSN 1432-0924.

[3] L. Ambrosio, V.M. Tortorelli, Approximation of functional depending on jumps by elliptic functional via t-convergence, Commun. Pure Appl. Math. 43 (8) (1990) 999–1036.

[4] H. Amor, J.J. Marigo, C. Maurini, Regularized formulation of the variational brittle fracture with unilateral contact: numerical experiments, J. Mech. Phys. Solids 57 (8) (2009) 1209–1229.

[5] P. Baluk, G. Gabella, Scanning electron microscopy of the muscle coat of the guinea-pig small intestine, Cell Tissue Res. 250 (3) (1987) 551–561.

[6] D. Balzani, S. Brinkhues, G.A. Holzapfel, Constitutive framework for the modeling of damage in collagenous soft tissues with application to arterial walls, Comput. Methods Appl. Mech. Eng. 213–216 (2012) 139–151.

[7] M. Bauer, E. Morales-Orcajo, L. Klemm, R. Seydewitz, V. Fiebach, T. Siebert, M. Böl, Biomechanical and microstructural characterisation of the porcine stomach wall: location- and layer-dependent investigations, Acta Biomater. 102 (2020) 83–99.

[8] C. Bellini, P. Glass, M. Sitti, E.S.D. Martino, Biaxial mechanical modeling of the small intestine, J. Mech. Behav. Biomed. Mater. 4 (8) (2011) 1727–1740.

[9] M.J. Borden, T.J.R. Hughes, C.M. Landis, M.A. Scott, C.V. Verhoosel, A phase–field description of dynamic brittle fracture, Comput. Methods Appl. Mech. Eng. 217–220 (2012) 77–95.

[10] B. Bourdin, G.A. Francfort, J.J. Marigo, Numerical experiments in revisited brittle fracture, J. Mech. Phys. Solids 48 (4) (2000) 797–826.

[11] B. Bourdin, G.A. Francfort, J.J. Marigo, The variational approach to fracture, J. Elast. Phys. Sci. Solids 91 (1) (2008) 5–148.

[12] A. Braides, Approximation of Free-discontinuity Problems, 1694, Springer Science & Business Media, 1998.

[13] E.L. Carniel, V. Gramigna, C.G. Fontanella, A. Frigo, C. Stefanini, A. Rubini, A.N. Natali, Characterization of the anisotropic mechanical behaviour of colonic tissues: experimental activity and constitutive formulation, Exp. Physiol. 99 (5) (2014) 759–771.

[14] E.L. Carniel, V. Gramigna, C.G. Fontanella, C. Stefanini, A.N. Natali, Constitutive formulations for the mechanical investigation of colonic tissues, J. Biomed. Mater. Res. Part A 102 (5) (2014) 1243–1254.

[15] E.L. Carniel, A. Rubini, A. Frigo, A.N. Natali, Analysis of the biomechanical behaviour of gastrointestinal regions adopting an experimental and computational approach, Comput. Methods Programs Biomed. 113 (1) (2014) 338–345.

[16] E.L. Carniel, A. Frigo, C.G. Fontanella, G.M. de Benedictis, A. Rubini, L. Barp, G. Pluchino, B. Sabbadini, L. Polese, A biomechanical approach to the analysis of methods and procedures of bariatric surgery, J. Biomech. 56 (2017) 32–41.

[17] S.L. Cartwright, M.P. Knudson, Evaluation of acute abdominal pain in adults, Am. Fam. Phys. 77 (7) (2008) 971–978.

[18] X. Chen, J. Zhao, H. Gregersen, The villi contribute to the mechanics in the guinea pig small intestine, J. Biomech. 41 (4) (2008) 806–812.

[19] P. Ciarletta, P. Dario, F. Tendick, S. Micera, Hyperelastic model of anisotropic fiber reinforcements within intestinal walls for applications in medical robotics, Int. J. Robot. Res. 28 (10) (2009) 1279–1288.

[20] C.M. Court-Brown, M.M. McQueen, S. Patterson-Brown, S.J. Nixon, Emergency surgical care in scotland, Surgeon 5 (2) (2007) 72–75.

[21] A. Delfino, N. Stergiopulos, J.E. Moore, J.J. Meister, Residual strain effects on the stress field in a thick wall finite element model of the human carotid bifurcation, J. Biomech. 30 (8) (1997) 777–786.

[22] H. Demiray, R.P. Vito, A layered cylindrical shell model for an aorta, Int. J. Eng. Sci. 29 (1) (1991) 47–54.

[23] Y. Dou, S. Gregersen, J. Zhao, F. Zhuang, H. Gregersen, Effect of re-feeding after starvation on biomechanical properties in rat small intestine, Med. Eng. Phys. 23 (8) (2001) 557–566.

[24] Y. Dou, S. Gregersen, J. Zhao, F. Zhuang, H. Gregersen, Morphometric and biomechanical intestinal remodeling induced by fasting in rats, Digest. Dis. Sci. 47 (5) (2002) 1158–1168.

[25] Y. Dou, J. Zhao, H. Gregersen, Morphology and stress-strain properties along the small intestine in the rat, J. Biomech. Eng. 125 (2) (2003) 266–273.

[26] Y. Dou, Y. Fan, J. Zhao, H. Gregersen, Longitudinal residual strain and stress-strain relationship in rat small intestine, Biomed. Eng. Online 5 (2006) 37.

[27] V.I. Egorov, I.V. Schastlivtsev, E.V. Prut, A.O. Baranov, R.A. Turusov, Mechanical properties of the human gastrointestinal tract, J. Biomech. 35 (10) (2002) 1417–1425.

[28] A.A. Eltayeb, M. Hashem, Management and outcome of neonatal bowel perforation, Ann. Pediatr. Surg. 4 (2008) 83–88.

[29] K. Fackler, L. Klein, A. Hiltner, Polarizing light microscopy of intestine and its relationship to mechanical behaviour, J. Microsc. 124 (Pt 3) (1981) 305–311.

[30] A. Ferrara, A. Pandolfi, A numerical study of arterial media dissection processes, Int. J. Fract. 166 (1) (2010) 21–33.

[31] G.A. Francfort, J.J. Marigo, Revisiting brittle fracture as an energy minimization problem, J. Mech. Phys. Solids 46 (8) (1998) 1319–1342.

[32] Y.C. Fung, K. Fronek, P. Patitucci, Pseudoelasticity of arteries and the choice of its mathematical expression, Am. J. Physiol.-Legacy Content 237 (5) (1979). H620-31.

[33] G. Gabella, The cross-ply arrangement of collagen fibres in the submucosa of the mammalian small intestine, Cell Tissue Res. 248 (3) (1987) 491–497.

[34] S.L. Gans, M.A. Pols, J. Stoker, M.A. Boermeester, Guideline for the diagnostic pathway in patients with acute abdominal pain, Digestive Surgery 32 (1) (2015) 23–31.

[35] C. Gao, H. Gregersen, Biomechanical and morphological properties in rat large intestine, J. Biomech. 33 (9) (2000) 1089–1097.

[36] T.C. Gasser, G.A. Holzapfel, Modeling the propagation of arterial dissection, Eur. J. Mech. - A/Solids 25 (4) (2006) 617–633.

[37] T. Gerasimov, L. de Lorenzis, On penalization in variational phase-field models of brittle fracture, Comput. Methods Appl. Mech. Eng. 354 (2019) 990–1026.

[38] M. Groenink, S.E. Langerak, E. Vanbavel, E.E. van Wall, B.J.M. Mulder, J.A.E. Spaan, A.C. van der wal, The influence of aging and aortic stiffness on permanent dilation and breaking stress of the thoracic descending aorta, Cardiovasc. Res. 43 (2) (1999) 471–480.

[39] K.E. Grund, G.P. Dzieniszewski, Gastrointestinale perforationen beim neugeborenen, Zeitschrift für Kinderchirurgie 32 (01) (1981) 56–68.

[40] O. Gültekin, H. Dal, G.A. Holzapfel, A phase-field approach to model fracture of arterial walls: theory and finite element analysis, Comput. Methods Appl. Mech. 312 (2016) 542–566.

[41] O. Gültekin, H. Dal, G.A. Holzapfel, Numerical aspects of anisotropic failure in soft biological tissues favor energy-based criteria: a rate-dependent anisotropic crack phase-field model, Comput. Methods Appl. Mech. Eng. 331 (2018) 23–52.

[42] O. Gültekin, S.P. Hager, H. Dal, G.A. Holzapfel, Computational modeling of progressive damage and rupture in fibrous biological tissues: application to aortic dissection, Biomech. Model. Mechanobiol. 18 (6) (2019) 1607–1628.

[43] H.W. Haslach, P. Riley, A. Molotsky, The influence of medial substructures on rupture in bovine aortas, Cardiovasc. Eng. Technol. 2 (4) (2011) 372–387.

[44] H.W. Haslach, L.N. Leahy, P. Fathi, J.M. Barrett, A.E. Heyes, T.A. Dumsha, E.L. McMahon, Crack propagation and its shear mechanisms in the bovine descending aorta, Cardiovasc. Eng. Technol. 6 (4) (2015) 501–518.

[45] H.W. Haslach, A. Siddiqui, A. Weerasooriya, R. Nguyen, J. Roshgadol, N. Monforte, E. Mc Mahon, Fracture mechanics of shear crack propagation and dissection in the healthy bovine descending aortic media, Acta Biomater. 68 (2018) 53–66.

[46] S.T. Herbert, S.F. Badylak, L.A. Geddes, B. Hillberry, G.C. Lantz, K. Kokini, Elastic modulus of prepared canine jejunum, a new vascular graft material, Ann. Biomed. Eng. 21 (6) (1993) 727–733.

[47] H. Hoeg, A. Slatkin, J. Burdick, W. Grundfest, Biomechanical modeling of the small intestine as required for the design and operation of a robotic endoscope, 2000.

[48] J. Hokanson, S. Yazdani, A constitutive model of the artery with damage, Mech. Res. Commun. 24 (2) (1997) 151–159.

[49] A.G. Holzapfel, Nonlinear solid mechanics II, 2000.

[50] G.A. Holzapfel, T.C. Gasser, R.W. Ogden, A new constitutive framework for arterial wall mechanics and a comparative study of material models, J. Elast. Phys. Sci. Solids 61 (1) (2000) 1–48.

[51] G.A. Holzapfel, G. Sommer, P. Regitnig, Anisotropic mechanical properties of tissue components in human atherosclerotic plaques, J. Biomech. Eng. 126 (5) (2004) 657–665.

[52] Z.G. Jia, W. Li, Z.R. Zhou, Mechanical characterization of stomach tissue under uniaxial tensile action, J. Biomech. 48 (4) (2015) 651–658.

[53] A. Karimi, R. Razaghi, M. Koyama, A patient-specific numerical modeling of the spontaneous coronary artery dissection in relation to atherosclerosis, Comput. Methods Programs Biomed. 182 (2019) 105060.

[54] J.H. Kim, S. Avril, A. Duprey, J.P. Favre, Experimental characterization of rupture in human aortic aneurysms using a full-field measurement technique, Biomech. Model. Mechanobiol. 11 (6) (2012) 841–853.

[55] L. Klemm, R. Seydewitz, M. Borsdorf, T. Siebert, M. Böl, On a coupled electro-chemomechanical model of gastric smooth muscle contraction, Acta Biomater. 109 (2020) 163–181.

[56] T. Komuro, The lattice arrangement of the collagen fibres in the submucosa of the rat small intestine: scanning electron microscopy, Cell Tissue Res. 251 (1) (1988) 117–121.

[57] C. Kuhn, R. Müller, A continuum phase field model for fracture, Eng. Fract. Mech. 77 (18) (2010) 3625–3634.

[58] J.T. Langell, S.J. Mulvihill, Gastrointestinal perforation and the acute abdomen, Med. Clin. N. Am. 92 (3) (2008) 599–625.

[59] D. Liao, J. Zhao, H. Gregersen, 3d mechanical properties of the partially obstructed guinea pig small intestine, J. Biomech. 43 (11) (2010) 2079–2086.

[60] H. Liao, S.M. Belkoff, A failure model for ligaments, J. Biomech. 32 (2) (1999) 183–188.

[61] S.H. Lu, M.S. Sacks, S.Y. Chung, D.C. Gloeckner, R. Pruchnic, J. Huard, W.C. de Groat, M.B. Chancellor, Biaxial mechanical properties of muscle-derived cell seeded small intestinal submucosa for bladder wall reconstitution, Biomaterials 26 (4) (2005) 443–449.

[62] X. Lu, J. Zhao, H. Gregersen, Small intestinal morphometric and biomechanical changes during physiological growth in rats, J. Biomech. 38 (3) (2005) 417–426.

[63] C.R. Macaluso, R.M. McNamara, Evaluation and management of acute abdominal pain in the emergency department, Int. J. Gener. Med. 5 (2012) 789–797.

[64] S.P. Marra, f.E. Kennedy, J.N. Kinkaid, M.F. Fillinger, Elastic and rupture properties of porcine aortic tissue measured using inflation testing, Cardiovasc. Eng. 6 (4) (2006) 123–131.

[65] J.R. Mathias, C.A. Sninsky, Motility of the small intestine: a look ahead, Am. J. Physiol.-Gastrointestinal Liver Physiol. 248 (5) (1985) G495–G500.

[66] A.L. Mescher, Mcgraw-hill education, Junqueira's basic histology: text and atlas(2018).

[67] C. Miehe, M. Hofacker, F. Welschinger, A phase field model for rate-independent crack propagation: Robust algorithmic implementation based on operator splits, Comput. Methods Appl. Mech. Eng. 199 (45) (2010) 2765–2778.

[68] P. Mitchell, J. Jakubowski, Failure testing cerebral arteries: are branch points weaker than unbranched vessels? Br. J. Neurosurg. 16 (6) (2002) 578–582.

[69] E. Morales-Orcajo, T. Siebert, M. Böl, Location-dependent correlation between tissue structure and the mechanical behaviour of the urinary bladder, Acta Biomater. 75 (2018) 263–278.

[70] K.H. Muhrer, R.D. Filler, 35. intestinale perforationen im neugeborenenalter, Langenbecks Archiv für Chirurgie 366 (1) (1985) 199–203.

[71] A.N. Natali, P.G. Pavan, E.L. Carniel, M.E. Lucisano, G. Taglialavoro, Anisotropic elasto-damage constitutive model for the biomechanical analysis of tendons, Med. Eng. Phys. 27 (3) (2005) 209–214.

[72] A.N. Natali, E.L. Carniel, P.G. Pavan, Constitutive modelling of inelastic behaviour of cortical bone, Med. Eng. Phys. 30 (7) (2008) 905–912.

[73] C. Noble, O. van der Sluis, R.M.J. Voncken, O. Burke, S.E. Franklin, R. Lewis, Z.A. Taylor, Simulation of arterial dissection by a penetrating external body using cohesive zone modelling, J. Mech. Behav. Biomed. Mater. 71 (2017) 95–105.

[74] J. Orberg, E. Baer, A. Hiltner, Organization of collagen fibers in the intestine, Connect. Tissue Res. 11 (4) (1983) 285–297.

[75] J.W. Orberg, L. Klein, A. Hiltner, Scanning electron microscopy of collagen fibers in intestine, Connect. Tissue Res. 9 (3) (1982) 187–193.

[76] C.A. Ordonez, J.C. Puyana, Management of peritonitis in the critically ill patient, Surg. Clin. N. Am. 86 (6) (2006) 1323–1349.

[77] S.K. Panda, M.L. Buist, A viscoelastic framework for inflation testing of gastrointestinal tissue, J. Mech. Behav. Biomed. Mater. 103 (2020) 103569.

[78] A. Parekh, A.D. Cigan, S. Wognum, R.L. Heise, M.B. Chancellor, M.S. Sacks, Ex vivo deformations of the urinary bladder wall during whole bladder filling: contributions of extracellular matrix and smooth muscle, J. Biomech. 43 (9) (2010) 1708–1716.

[79] S. Pasta, J.A. Phillippi, T.G. Gleason, D.A. Vorp, Effect of aneurysm on the mechanical dissection properties of the human ascending thoracic aorta, J. Thorac. Cardiovasc. Surg. 143 (2) (2012) 460–467.

[80] B. Patel, H. Chen, A. Ahuja, J.F. Krieger, J. Noblet, S. Chambers, G.S. Kassab, Constitutive modeling of the passive inflation-extension behavior of the swine colon, J. Mech. Behav. Biomed. Mater. 77 (2018) 176–186.

[81] J.A. Peña, M.A. Martínez, E. Peña, Failure damage mechanical properties of thoracic and abdominal porcine aorta layers and related constitutive modeling: phenomenological and microstructural approach, Biomech. Model. Mechanobiol. 18 (6) (2019) 1709–1730.

[82] K. Pham, H. Amor, J.J. Marigo, C. Maurini, Gradient damage models and their use to approximate brittle fracture, Int. J. Damage Mech. 20 (4) (2010) 618–652.

[83] S. Puértolas, E. Peña, A. Herrera, E. Ibarz, L. Gracia, A comparative study of hyperelastic constitutive models for colonic tissue fitted to multiaxial experimental testing, J. Mech. Behav. Biomed. Mater. 102 (2020) 103507.

[84] A. Raina, C. Miehe, A phase-field model for fracture in biological tissues, Biomech. Model. Mechanobiol. 15 (3) (2016) 479–496.

[85] M.K. Rausch, G.E. Karniadakis, J.D. Humphrey, Modeling soft tissue damage and failure using a combined particle/continuum approach, Biomech. Model. Mechanobiol. 16 (1) (2017) 249–261.

[86] J.F. Rodríguez, F. Cacho, J.A. Bea, M. Doblaré, A stochastic-structurally based three dimensional finite-strain damage model for fibrous soft tissue, J. Mech. Phys. Solids 54 (4) (2006) 864–886.

[87] M.S. Sacks, D.C. Gloeckner, Quantification of the fiber architecture and biaxial mechanical behavior of porcine intestinal submucosa, J. Biomed. Mater. Res. Part A 46 (1) (1999) 1–10.

[88] M. Schietroma, S. Cappelli, F. Carlei, A. Pescosolido, N. Lygidakis, G. Amicucci, Acute abdomen: early laparoscopy or active laparotomic- laparoscopic observation? Hepato-Gastroenterology 54 (2007) 1137–1141.

[89] N.H. Scott, The incremental bulk modulus, young's modulus and poisson's ratio in nonlinear isotropic elasticity: physically reasonable response, Math. Mech. Solids 12 (5) (2007) 526–542.

[90] R. Seydewitz, R. Menzel, T. Siebert, M. Böl, Three-dimensional mechano-electrochemical model for smooth muscle contraction of the urinary bladder, J. Mech. Behav. Biomed. Mater. 75 (2017) 128–146.

[91] D.P. Sokolis, Multiaxial mechanical behaviour of the passive ureteral wall: experimental study and mathematical characterisation, Comput. Methods Biomech. Biomed. Eng. 15 (11) (2012) 1145–1156.

[92] D.P. Sokolis, Experimental study and biomechanical characterization for the passive small intestine: identification of regional differences, J. Mech. Behav. Biomed. Mater. 74 (2017) 93–105.

[93] D.P. Sokolis, Variation of passive biomechanical properties of the small intestine along its length: microstructure-based characterization, Bioengineering 8 (3) (2021) 32.

[94] D.P. Sokolis, I.K. Orfanidis, M. Peroulis, Biomechanical testing and material characterization for the rat large intestine: regional dependence of material parameters, Physiol. Meas. 32 (12) (2011) 1969–1982.

[95] D.P. Sokolis, S.G. Sassani, Microstructure-based constitutive modeling for the large intestine validated by histological observations, J. Mech. Behav. Biomed. Mater. 21 (2013) 149–166.

[96] G. Sommer, T.C. Gasser, P. Regitnig, M. Auer, G.A. Holzapfel, Dissection properties of the human aortic media: an experimental study, J. Biomech. Eng. 130 (2) (2008).

[97] G. Sommer, S. Sherifova, P.J. Oberwalder, O.E. Dapunt, P.A. Ursomanno, A. De Anda, B.E. Griffith, G.A. Holzapfel, Mechanical strength of aneurysmatic and dissected human thoracic aortas at different shear loading modes, J. Biomech. 49 (12) (2016) 2374–2382.

[98] A.J.M. Spencer, I. Theory, Part II of invariants, Contin. Phys. 1 (1971) 239–353.

[99] D. St-Vil, G.L. Bouthillier, F.I. Luks, A.L. Bensoussan, H. Blanchard, S. Youssef, Neonatal gastrointestinal perforations, J. Pediatr. Surg. 27 (10) (1992) 1340–1342.

[100] D. Sun, J. Zhao, D. Liao, P. Chen, H. Gregersen, Shear modulus of the partially obstructed rat small intestine, Ann. Biomed. Eng. 45 (4) (2017) 1069–1082.

[101] E. Tanné, T. Li, B. Bourdin, J.-J. Marigo, C. Maurini, Crack nucleation in variational phase-field models of brittle fracture, J. Mech. Phys. Solids 110 (2018) 80–99.

[102] S. Teichtmeister, D. Kienle, F. Aldakheel, M.A. Keip, Phase field modeling of fracture in anisotropic brittle solids, Int. J. Non-Linear Mech. 97 (2017) 1–21.

[103] J. Tong, T. Cohnert, P. Regitnig, G.A. Holzapfel, Effects of age on the elastic properties of the intraluminal thrombus and the thrombus-covered wall in abdominal aortic aneurysms: biaxial extension behaviour and material modelling, Eur. J. Vasc. Endovasc.Surg. 42 (2) (2011) 207–219.

[104] J. Tong, G. Sommer, P. Regitnig, G.A. Holzapfel, Dissection properties and mechanical strength of tissue components in human carotid bifurcations, Ann. Biomed. Eng. 39 (6) (2011) 1703–1719.

[105] J. Tong, A.J. Schriefl, T. Cohnert, G.A. Holzapfel, Gender differences in biomechanical properties, thrombus age, mass fraction and clinical factors of abdominal aortic aneurysms, Eur. J. Vasc. Endovasc. Surg. 45 (4) (2013) 364–372.

[106] R. Trostorf, E. Morales-Orcajo, T. Siebert, M. Böl, Location- and layer-dependent biomechanical and microstructural characterisation of the porcine urinary bladder wall, J. Mech. Behav. Biomed. Mater. 115 (2021) 104275.

[107] O. van Ruler, M.A. Boermeester, Surgical treatment of secondary peritonitis: acontinuing problem, Der Chirurg 88 (Suppl 1) (2017) 1–6.

[108] L. Wang, N.A. Hill, S.M. Roper, X. Luo, Modelling peeling- and pressure-driven propagation of arterial dissection, J. Eng. Math. 109 (1) (2018) 227–238.

[109] T. Wu-Prisacari, A. Carpiuc, M. Poncelet, L. de Lorenzis, Phase-field simulation of interactive mixed-mode fracture tests on cement mortar with full-field displacement boundary conditions, Eng. Fract. Mech. 182 (2017) 658–688.

[110] L. Zanelli, A. Montanaro, E.L. Carniel, P.G. Pavan, A.N. Natali, The study of equivalent material parameters in a hyperelastic model, Int. J. Non-Linear Mech. 89 (2017) 142–150.

[111] J. Zhao, D. Liao, J. Yang, H. Gregersen, Biomechanical remodelling of obstructed guinea pig jejunum, J. Biomech. 43 (7) (2010) 1322–1329.

[112] J. Zhao, D. Liao, J. Yang, H. Gregersen, Stress and strain analysis of contractions during ramp distension in partially obstructed guinea pig jejunal segments, J. Biomech. 44 (11) (2011) 2077–2082.

[113] Y. Zhao, S. Siri, B. Feng, D.M. Pierce, Computational modeling of mouse colorectum capturing longitudinal and through-thickness biomechanical heterogeneity, J. Mech. Behav. Biomed. Mater. 113 (2021) 104127.